Seismic Imaging of a Granitoid-Greenstone Boundary in the Paleoarchean Pilbara Craton

Anusha Prasad

Thesis submitted to the Faculty of the
Virginia Polytechnic Institute and State University
in partial fulfillment of the requirements for the degree of

Master of Science
in
Geoscience

John A. Hole, Chair
W. Steven Holbrook
Mark J. Caddick

February 7th, 2023
Blacksburg, Virginia

Keywords: Seismic reflection imaging, steep dips, Kirchhoff migration, Paleoarchean tectonics, Pilbara Craton

Seismic Imaging of a Granitoid-Greenstone Boundary in the Paleoarchean Pilbara Craton

Anusha Prasad

(ABSTRACT)

The mode of tectonics by which early Archean proto-continents were deformed was investigated in the Pilbara Craton in Western Australia, which has not been substantially tectonically deformed since ∼3.2 Ga. The craton consists of a unique dome and keel structure where vertical, low-grade metamorphism basaltic greenstone keels surround large granitic (TTG) domes. The dominant model for 3.5-3.2 Ga deformation in the Pilbara is gravity-driven vertical tectonics, or partial convective overturn in a hot crust. In this model, the granitic bodies rose upward as solid-state diapirs, and the greenstones "sagducted" downward around the granitic bodies. Australian scientists acquired deep seismic reflection data crossing a granitoid-greenstone boundary. Their processing did not image the geologically mapped steep dip of the boundary because standard methods limit the maximum dip. A 37-km section of these data were reprocessed using 2D Kirchhoff prestack depth migration to include vertical dips. The western half of the migrated section images a granitoid dome with weak to no reflectivity that extends deeper than 4 km. The eastern half images 2-3 km of layered volcanic rocks of the Fortescue Group overlying the greenstones. Seismic velocity models created using travel-time tomography suggest a thin weathering layer overlying slightly fractured crystalline rocks. These fractures close within 200-300 m depth, and velocity reaches bedrock speeds consistent with expected values of granitoids to the west and volcanic rocks of the Fortescue Group to the east. The best migrated image contains several

reflections with dips ($\sim$45-55°) cross-cutting each other from both directions at the location of the expected granitoid-greenstone boundary. This strongly suggests the presence of steep dips in the upper $\sim$1.5 km but does not provide a definitive image. This inconclusive result is due to strong surface-wave noise, the crooked 2D seismic line, and the 3D nature of the geologic boundary at the seismic line. A very small seismic velocity gradient within the crystalline bedrock limits the maximum depth to which vertical features can be imaged.

Seismic Imaging of a Granitoid-Greenstone Boundary in the Paleoarchean Pilbara Craton

Anusha Prasad

(GENERAL AUDIENCE ABSTRACT)

The Pilbara craton is one of the few exposed and intact pieces of continents that were formed $\sim$ 3.2 billion years ago. This research analyzes how these early land masses were deformed. There are two methods by which early land masses evolved—vertical tectonics (a more rudimentary, gravity-driven form of plate movement) or horizontal tectonics (which is closer to modern-day tectonics and requires many stages of deformation). This area has a unique dome-and-keel structure where greenstones (metamorphosed volcanics) are vertically wrapped around large granitic domes. Studying the vertical features of the greenstones will allow us to ascertain how tectonics evolved in the area. A seismic survey was conducted in 2018 in the area. These data were reprocessed to include steep dips to extract the exact location of the steeply dipping boundary between the dome and keel structure at depth. The resulting image contains inconclusive evidence due to the physical limitations of the geology and the sharp bend in the seismic line. Further studies need to be done to determine if the Pilbara Craton was formed by vertical tectonics.

Dedication

I would like to thank my advisor, Dr. John A. Hole for his support and advise throughout my time at Virginia Tech. I would also like to thank my committee members, Dr. Steve Holbrook and Dr. Mark Caddick, for their valuable insights. I would like to thank many people in the Department of Geoscience for their help during my two years at Virginia Tech. A special thanks goes to all the friends I made in Blacksburg–Claire, Alyssa, Mary Anne, Nicole, and Abby. I could not have done this without your support. Thank you for being such great friends and especially for listening to me complain about my research when I was stressed. Thanks to my best friends–Bailey, Megan, and Caitlin. Your unconditional love and support (even from thousands of miles away) is and always will be appreciated. Lastly, I would like to thank my parents, Bimal and Rajat Rekha Prasad. Thank you for all that you have done for me. I would not be here if it was not for all your encouragement and support.

Acknowledgments

I would like to acknowledge Tanya Fomin (Geoscience Australia) for assistance in accessing the data, Andrew Calvert (Simon Fraser University) for helpful conversations about the data, and Basil Tikoff (University of Wisconsin, Madison) for inspiring the project. A special acknowledgement to James Dunson for computer assistance. Software support was provided by Landmark Software and Services, a Halliburton Company. The Department of Geological Sciences of Virginia Tech has aided in this research project through the Petroleum Industry Summer Scholarship and by providing teaching assistantships during my studies.

Contents

List of Figures

List of Tables

Chapter 1

Introduction

The mechanics of the lithosphere, the rigid outer layer of the Earth consisting of the upper and lower crust, are responsible for the formation and destruction of the global network of plates and their boundaries (*Kearey et al.*, 2009). The lithosphere keeps a record of the formation as well as the dismantling of these plates; however, it remains difficult to access these records due to the frequent destruction of plates by tectonic processes. Significant debate remains in the scientific community about the origins of plate tectonics and the mechanisms by which the Earth's earliest proto-continents, formed in the early Archean (<4-3.2 Ga), have evolved. Times proposed for the origin of plate tectonics ranges from the Hadean[1] (*Hopkins et al.*, 2008, 2010; *Harrison*, 2009) to the late Proterozoic (*Stern*, 2005). The mechanisms, or the tectonics modes, by which the Earth's earliest proto continents may have evolved and deformed before the commencement of modern-day plate tectonics are much debated (*Van Kranendonk et al.*, 2007; *Smithies et al.*, 2007; *Brown et al.*, 2020).

An ideal location to study the mechanisms by which the earliest proto-continents evolved is the Pilbara Craton in Western Australia (Figure: 7.1). The Pilbara Craton is one of the few exposed and mostly intact early Archean cratons on the planet (Figure: 7.2). Structural mapping and seismic reflection imaging in global Archean belts show evidence of horizontal plate-like tectonics (tectonics processes requiring multiple stages of deformation similar to a more modern-day system of plate tectonics) by the Mesoarchean (∼2.7 Ga) (*Calvert et al.*,

[1]Geological timeline used in this manuscript listed in Appendix A

1995; *White et al.*, 2003). The Pilbara Craton has not been tectonically deformed since ~3.2 Ga, making it an ideal location to study deformation that may have preceded plate tectonics. The Pilbara Craton has a dome and keel structure where large granitoid bodies "domes" are surrounded by vertical low-grade metamorphosed basalt units (greenstone "keels"). There is broad but not complete consensus that these structures in the Pilbara Craton are evidence for gravity-driven, vertical tectonics (*Collins*, 1989; *Collins and Van Kranendonk*, 1989; *Francois et al.*, 2014).

An 872-km-long deep crustal seismic reflection survey was recently acquired across most of Western Australia by government agencies (*Fomin and Costelloe*, 2019). The western end of the seismic survey extends into the Pilbara Craton and crosses a granitoid-greenstone boundary. Standard seismic reflection methods along with the initial data processing and interpretation of these data did not include vertical dips like those observed structurally near the granitoid-greenstone boundaries. These data are reprocessed to include steep dips by implementing Kirchhoff prestack depth migration. The goal is to establish the dip of the dome and keel structures at depth to determine whether these structures were due to vertical or horizontal plate-like deformation.

Chapter 2

Background

2.1 Origin of Plate Tectonics

Most scientists theorize the origin of plate tectonics dates back to the Archean (*Cawood et al.*, 2006; *Hawkesworth et al.*, 2017), but some argue as early as the Hadean (*Hopkins et al.*, 2008; *Harrison*, 2009) or as late as the late Proterozoic (*Stern*, 2005). Earth's earliest cratons date to the early Archean (Figure: 7.2, 7.3), and thus the earliest cratons may have pre-dated plate tectonics. The magmatic and structural mechanisms by which early proto-continents emerged and subsequently deformed are still under considerable debate (Figure: 7.4).

The operation of plate tectonics before the Proterozoic remains contentious. Part of the debate is because the petrological, geochemical, structural, geophysical, and metamorphic signatures of plate tectonics could have been different in Archean crust simply because Earth was hotter (*Korenaga*, 2013). Another reason the origin of plate tectonics remains debated is that the oceanic lithosphere has been mostly destroyed by plate tectonics, and there is simply not enough preserved continental lithosphere. Approximately fifty percent of the exposed rocks in the continental crust are younger than 600 Ma; less than five percent are older than 3.0 Ga, and rocks older than 3.6 Ga are incredibly rare (Figure: 7.3) (*Goodwin*, 1996). Much of what remains of the early proto-continents has been periodically deformed and metamorphosed by younger plate tectonics.

The lack of records preserved in Archean rocks hinders the argument for the origin of plate tectonics before this period and is one of the driving forces for debate on this topic within the community. Evidence of zircons dates to 4.2 Ga, and some have theorized that this is evidence for subduction and plate tectonics at that time (*Hopkins et al.*, 2008, 2010; *Harrison*, 2009; *Turner et al.*, 2014; *Foley*, 2018). Some isotopic and trace element evidence for mantle and crustal processes implies the onset of plate tectonics and subduction as early as 3.9 Ga (*Shirey et al.*, 2008). Still, many global geochemical studies suggest ∼3 Ga as the onset of plate tectonics (*Dhuime et al.*, 2012; *Hawkesworth et al.*, 2017). Stratigraphic and geochemical evidence indicates the beginning of Paleoarchean tectonics in West Greenland by ∼3.6 Ga (*Nutman et al.*, 2002). Paleomagnetic, geochemical, and structural deformation evidence suggests plate tectonics in a few Archean cratons since 3.1 Ga (*Cawood et al.*, 2006) and in many cratons by 2.7 Ga (*Condie and Kroner*, 2008). Paired high-pressure, low-temperature and low-pressure, high-temperature metamorphic belts marks the beginning of modern-day continental evidence for subduction and plate tectonics by 2.8 Ga (*Brown*, 2006). A lack of geological evidence for ultra-high-pressure metamorphism and ophiolites have been argued as evidence that plate tectonics did not exist before ∼1 Ga (*Stern*, 2005).

2.2 Archean Cratons

The isotopic composition of Hadean zircons from the Jack hills regions of Australia suggests that the Earth's surface and interior had cooled and stabilized enough by 4.2 Ga to create ancient felsic rocks that could be a part of a proto-continental crust (*Cavosie et al.*, 2005). However, no Hadean rocks are known and the earliest preserved proto-continents formed in the Paleoarchean (Figure: 7.3). By the Archean, portions of the subcontinental lithospheric mantle were mainly composed of dehydrated, highly magmatically depleted mantle peri-

dotite. This depleted peridotite caused these Archean fragments to be buoyant and strong lithosphere, creating the first stable continental cratons (*Kusky and Polat*, 1999). These cratons are now at the core of many continental interiors (Figure: 7.2). However, only portions of the Archean cratons are exposed, as Archean continental crust is often deformed, metamorphosed, and buried beneath Proterozoic sedimentary and volcanic rocks (*Goodwin*, 1996).

The Archean continental crust consists of low-grade metamorphosed basaltic greenstone belts, large granitic bodies, and locally higher-grade felsic gneiss terranes (*Windley and Bridgwater*, 1971). The extensive greenstone belts consist of metamorphosed mafic volcanic and interbedded sedimentary sequences, and they generally surround the plutonic rocks and gneisses. High mantle temperatures promote intensive plume activity due to higher temperatures at the core-mantle boundary (*Smithies et al.*, 2005). This causes a higher percentage of partial melt than modern mantle melting resulting in the composition of these greenstone belts being more mafic, including an abundance of ultramafic komatiite, which is rare in the post-Archean rock record (*Kusky and Polat*, 1999).

The large granitic plutonic bodies consist of tonalite, trondhjemite, and granodiorite (TTG). This TTG series is distinct from modern-day subduction-zone and collision-zone granitic complexes in that they have less potassium feldspar, indicating the melting of a more primitive basaltic source (*Martin*, 1993). The source for the TTGs was partial melting of either subducting hydrated oceanic crust (*Smithies et al.*, 2007) or a thick hydrated volcanic crustal lid in a high geothermal gradient (*Moore and Webb*, 2013). The former requires plate tectonics, while the latter does not. The felsic gneiss terranes are consistent with metamorphosed TTGs (*Windley and Bridgwater*, 1971).

Exposed portions of the Archean crust, particularly those in western Australia and southern Africa, suggest a structural geometry between the TTGs and greenstones where large granitic

bodies, called "domes," are structurally surrounded by steeply dipping greenstone "keels" that are layered parallel to the boundaries. This structural relationship suggests a mode of deformation in the early Archean that does not resemble plate tectonics (*Van Kranendonk et al.*, 2010). While Archean crust elsewhere is not inconsistent with such a structural relationship, younger collisional tectonics usually overprints the TTG-greenstone boundaries.

2.3 East Pilbara Terrane

The 3.53-2.83 Ga East Pilbara terrane in Western Australia (Figure: 7.1) is one of the few intact and exposed dome and keel structures. The East Pilbara terrane comprises large, evenly spaced granitic domes surrounded by variably deformed greenstones. These greenstones are metamorphosed volcano-sedimentary sequences that are steeply dipping and strongly deformed at the granitoid-greenstone boundary (*Hickman and Van Kranendonk*, 2004; *Roberts et al.*, 2022). Deformation decreases farther away from the domes, and there are preserved volcanic structures, including pillow basalts. The greenstones include cyclic sequences of basalts, komatiites, volcaniclastics, felsic volcanics, chert members, and banded iron formations (*Van Kranendonk*, 2006). The greenstones within the East Pilbara terrane include three component groups—the Warrawoona Group (3.53 to 3.42 Ga), the Kelly Group (3.35-3.31 Ga), and the Sulphur Springs Group (3.27 to 3.23 Ga) (*Hickman and Van Kranendonk*, 2012). The end of each group is marked by a period of erosional unconformity.

The granitic domes are of the tonalite-trondhjemite-granodiorite (TTG) suite and are divided into supersuites–Callina/Tambina (3.47-3.42 Ga), Emu Pool (3.32-3.29 Ga), and Cleland (3.28-3.23 Ga). Supersuites either predate or coincide with the deduced timing of dome and keel deformation (*Hickman*, 2012). The volcanic supersuites in the greenstones roughly correlate in time with the 3.5-3.2 Ga granitic supersuites. The undeformed Split Rock

supersuite is proposed to have been formed sometime between 2.89-2.83 Ga due to thermal events that occurred after the formation of the domes. The dome and keel structures were eroded to near their present exposure level, then overlain by gently tilted 2.78-2.45 Ga Fortescue and Hamersley flood basalts (*Hickman and Van Kranendonk*, 2012). The older dome and keel structures are well exposed in the northern Pilbara province but remain deeply covered in the southern Pilbara province (Figure 7.1).

As most of the >3.2 Ga East Pilbara terrane has not been tectonically modified and is very well exposed, this area has been studied extensively and used as the archetype to investigate the mode of deformation that formed dome and keel structures. This architecture is indicative of Paleoarchean crust (*Hickman*, 1984). It contains records of deformation that could have predated continental crust growth and movement during the Mesoarchean and Neoarchean (*Van Kranendonk et al.*, 2010; *Dhuime et al.*, 2012). The location of this research is the eastern edge of the 3.47-2.83 Ga Mount Edgar dome (Figure: 7.5). This granitic dome has an ovoid shape approximately 50 km in diameter. The granitoid-greenstone boundary is variably deformed, with the strongest deformation at the southwest boundary. Volcanic layering in the greenstones surrounding the dome is vertical and parallel to the boundary, wrapping the entire dome. Sub-vertical shear foliation and lineation near the margins of the Mount Edgar dome developed under high-temperature solid-state conditions with minor partial melt, such that the dome resembles a rising ductile diapir (*Collins*, 1989; *Roberts et al.*, 2022). The greenstones are only locally exposed around the northern and western margins of the dome, where the Fortescue Group extends to the dome boundary and overlies most of the greenstone. Unfortunately, the data for this study is at the eastern margin, where greenstone exposure is sparse due to overlying Fortescue rocks (Figure: 7.6).

There is broad but not unanimous consensus in the scientific community that studies the Pilbara craton that buoyancy-driven, non-plate tectonic processes created the dome and

keel structures (*Hickman and Van Kranendonk*, 2004; *Van Kranendonk et al.*, 2007, 2010; *Smithies et al.*, 2007; *Brown et al.*, 2020). Since these structures predate direct evidence for plate tectonics and the preferred $\sim$ 3 Ga date of many studies, dome and keel deformation processes may predate plate tectonics. However, they do not preclude earlier or concurrent plate tectonic deformation elsewhere. In any case, they represent a unique deformation mode that existed in Earth's earliest continental crust, and they are informative about the early pressure-temperature conditions in Archean proto-continents.

The dominant model to explain the dome and keel structures involves vertical gravity-driven partial convective overturn (Figure: 7.7) (*Collins*, 1989; *Collins and Van Kranendonk*, 1989; *Van Kranendonk et al.*, 2007; *Smithies et al.*, 2007; *Francois et al.*, 2014). During 3.5-3.2 Ga, periodic mantle plume activity created widespread partial melt conditions within the older crust to create voluminous TTG intrusions and extruded thick surface deposits of mafic volcanic rocks–the roughly correlative granitoid and greenstone supersuites. The granitic rocks were overlain by up to 10 km of much denser mafic volcanic rocks at a time in Earth's history when the geothermal gradient was much higher than today. The deposition created a negatively buoyant crust, and convective overturn triggered by widespread thermal softening in the area caused the granitic domes to diapir up in the solid state and denser layered volcanic greenstones "sagducted" downward. This created granitic "domes" and steep, deep greenstone "keels." Steeply plunging lineations within the vertical volcanic layers of the greenstones and within the margins of the Mount Edgar dome indicate vertical solid-state deformation (*Hickman*, 1984; *Hickman and Van Kranendonk*, 2004; *Roberts et al.*, 2022). The timing of dome and keel deformation is loosely constrained to occur during and immediately after each granitic and corresponding volcanic supersuite, which provided both new rocks to drive density forces in high crustal temperatures.

Other models for the dome and keel structures have been proposed that involve large-scale

horizontal extension or compression consistent with far-field plate tectonic driving forces. *Zegers et al.* (1996) suggested a model that involved horizontal contraction followed by horizontal extensional core complex deformation. *Kloppenburg et al.* (2001) proposed more than one sequence of horizontal contraction followed by horizontal extension (Figure: 7.8). *Blewett* (2002) suggested multiple stages of contraction in different directions to create fold interference (Figure: 7.9). Each of these models requires multiple stages of deformation in different directions to produce 3D ovoid domes surrounded by greenstones rather than the 2D structures that are produced by a single phase of horizontal contraction or extension. A single episode of horizontal deformation would also result in uni-axial lineations with the same sense of movement across the domes, unlike the observed radially symmetric foliations and lineations created by vertical tectonics. (*Hickman and Van Kranendonk*, 2004).

Chapter 3

Kidson Seismic Reflection Data

3.1 Data Acquisition

Geoscience Australia acquired deep seismic reflection data as a part of the Exploring for the Future (EFTF) program in collaboration with the Geological Survey of Western Australia (*Fomin and Costelloe*, 2019; *Doublier et al.*, 2020; *Carr et al.*, 2022). The 872-km-long Kidson seismic line acquired in 2018 crossed a large portion of the Canning Basin in Western Australia (Figure: 7.10). It covers the Kidson Sub-basin in the east and extends into the Pilbara Craton in the west. This deep crustal seismic reflection survey was acquired to map the geology and regional context of a remote portion of the Canning Basin and to assess energy, mineral, and groundwater resources in the area. The seismic source, three vibrators, was centered over a 12 km geophone spread, making the maximum source to receiver offset 6 km. The data were recorded using a geophone array designed to attenuate low-velocity surface wave noise. Vibrator-point and receiver station spacing were 40 and 20 m, respectively. Detailed acquisition parameters for the survey are listed in Table 8.1.

3.2 Previous Work

The seismic reflection data (Figure: 7.11) were processed by an Australian team using standard industry methods (*Fomin and Costelloe*, 2019; *Doublier et al.*, 2020; *Carr et al.*, 2022).

The processing scheme utilized by the Australian team produced separate images focused on the sedimentary Canning Basin and on the deep crustal structure. Crooked line geometry was applied since the road had some sharp bends. Approximately 1.37% of the data set was deleted due to high amplitude noise from trucks and near the seismic source. A frequency-wavenumber domain fan filter was applied to eliminate linearly coherent, high amplitude, source-generated S-wave and surface-wave noise. Refraction static corrections were applied to a reference datum of 500 m above sea level. Prestack time migration, prestack depth migration, and poststack migration streams were utilized. The shallow sections were migrated with a 20 km aperture, and the deeper sections were migrated with a 40 km aperture. A 70 $^\circ$ aperture was applied to image steeper structures at depth.

Doublier et al., 2020 interpreted the deep crustal structure along the line. The westernmost portion of the migrated seismic section of the line that crosses into Mount Edgar dome is shown in Figure 7.11. Near the surface, the Fortescue Group volcanic rocks are imaged in the eastern half of Figure 7.11 to a maximum depth of 2-4 km, with internal reflections showing the bases of formations within the group. Due to its crystalline structure, the granitoid dome at the line's western end is not expected to be highly reflective, but there are some reflections within hundreds of meters of the surface. These may represent deep weathering. The Fortescue basin sharply terminates in the seismic image at its mapped western edge, which coincides with the mapped location of the granitoid-greenstone boundary. There is no reflection from the granitoid-greenstone boundary itself, which is locally geologically steep and should be a highly reflective geologic contrast, but steep dips (>70 $^\circ$) were not migrated. I will attempt to image steeper dips to image this structure.

The section of the upper crust below ∼1-3 km is non-reflective in granitoids and greenstones underlying the Fortescue (Figure 7.11). This non-reflective phenomenon is typical of large granitic bodies. The greenstones are strongly layered but vertical near the mapped granitoid-

greenstone boundary; therefore, they may be transparent due to steepness or structural complexity at depth. There are high-amplitude, laterally continuous reflectors in the middle crust, with some crossing beneath the granitoid-greenstone boundary. This suggests the granitic dome structure does not extend deeper than ∼15 km vertically. The lower crust is highly reflective, with many short reflectors. The Mohorovčić discontinuity (Moho) is represented by the base of lower crustal reflectivity at ∼30 km depth above the non-reflective lithospheric upper mantle.

Chapter 4

Imaging Steep Dips

4.1 Turning Waves

Whenever seismic velocity increases with depth, seismic energy is refracted into horizontal ray paths at a certain depth before returning to the surface. These refracted rays, also known as turning rays, can reflect off steep boundaries to return to the surface (Figure: 7.12B) (*Hale et al.*, 1992; *Hole et al.*, 1996, 2001). Turning-wave reflections can constrain the steep boundary to the maximum depth of the turning waves, which depends on the vertical velocity gradient. The path of these turning rays causes reflection time to increase as source-receiver offset decreases, a horizontal back-scattering results in the reflections exhibiting abnormal, non-hyperbolic moveout in shot and common midpoint (CMP) gathers. This abnormal moveout, combined with conventional methods of seismic reflection processing that emphasize shallow dips, prevents imaging steeper dips in the existing migrated image (Figure: 7.11) (*Hale et al.*, 1992). Since conventional poststack seismic processing assumes normal moveout, prestack depth migration is essential to image steep dips.

The granitoid-greenstone boundary is mapped as steeply dipping near the seismic line (*Roberts et al.*, 2022) but is not observed as a reflection in the previously processed seismic data (Figure: 7.11), possibly because standard reflective processes are designed to image horizontal reflectors, and, in this case because the processing was limited to 70 $^\circ$ dips. There is evidence of abnormal moveout in shot gathers near the surface location of the granitoid-

greenstone boundary. Due to the strong surface-wave energy (Figure: 7.13), it's not obvious in the shot gathers whether this abnormal moveout is from P-waves or back-scattered surface waves. Therefore, the data need to be reprocessed with prestack migration to include steep dips.

4.2 Travel-time Tomography

An accurate velocity model is required for prestack depth migration to image steeply dipping structures. Travel-time tomography can utilize first arrival refraction information from the same seismic reflection survey to create a velocity model of shallow structure, but deeper structure may need data with longer source-receiver offsets. If ray coverage is ideal and inversion parameters are chosen to bias towards a minimum-structure result, the resulting velocity model can be a smoothed version of the actual subsurface structure (*Zelt*, 1999). Such a smoothed velocity model is ideal for prestack depth migration.

First arrival travel-times were picked for all the shot gathers in the portion of interest of the seismic reflection line. The raw vibrator point gathers show first arrival P-waves are traveling at 5000-6000 km/s at longer source-receiver offsets (Figure: 7.13). Slower apparent velocities are only observed at very short offsets of <200 m. These data were inverted using the algorithm of *Hole* (1992) using a scheme that biases towards a minimum-structure result. A finite-difference solution to the Eikonal equation is employed to calculate first-arrival travel times. The velocity model is parameterized into a uniform grid with constant velocity values, and first arrival travel-times are computed for all grid points within the model for each source. Rays are found by tracing backwards from each receiver through the gridded travel-time field to the source. The travel-time misfit is used to update the velocity model using simple backprojection. A smoothing factor that decreases as the model converges is applied to the

model perturbation during each iteration. The seismic tomography problem is nonlinear because the ray paths depend upon the velocity model. The nonlinear problem is solved by updating the velocity model, re-computing times and rays, and iterating. Forward modeling between each backprojection becomes increasingly important as the spatial resolution of the model improves, and the allowable magnitude of slowness perturbations decreases because the linearization of this problem relies on the stability of the ray's positions. Slowly reducing the smoothing as the model converges pushes the misfits into large-scale structure, producing a minimum-structure model that fits the data.

A good starting velocity model is essential to the travel-time tomography process due to the strong nonlinearity of the problem. In addition, it can stabilize the velocity model in the areas where ray coverage is limited. A starting velocity model that increases with depth is essential to ensure that raypaths return to the surface to create an accurate starting model. A 1D velocity model was created manually. First breaks were picked and averaged across three shots gathers east and west of the proposed boundary to represent the difference in velocity between the granitoids and the younger basalts of the Fortescue Group. A 1D layered velocity model was calculated from the first arrival picks for each side of the granitoid-Fortescue boundary (Figure: 7.14). These 1D velocity models insinuate that there is a thin layer of weathered rocks with lower velocity and that velocity quickly increases to values expected for hard rock with minor fractures ($\sim$ 4000 m/s) within tens of meters of the surface. Velocities increase to unfractured values within a few hundred meters of the surface. The two models suggest that the bedrock velocity in the top hundreds of meters is faster in the granitoids than in the Fortescue.

The average compressional wave velocity at 5 km depth in granitic rocks is 6100 m/s, and low to medium grade metamorphosed basalt is 6300-6650 m/s, increasing with grade (*Christensen and Mooney*, 1995). Given the information from the 1D velocity models (Figure:

7.14) and expected velocities at depth, a suite of reasonable starting models was created for tomography. The starting velocity model can heavily influence the tomography velocity model, so the large-to-small smoothing scheme was used to assess and reduce this dependency. Several different starting velocity models, smoothing horizontal-to-vertical aspect ratios, final smoothing size, and a number of iterations were tested to create a preferred velocity model (Figure: 7.15B). A starting velocity model with shallow speeds of ∼4500 m/s increasing to 6000 m/s at ∼ 1.2 km depth was chosen (Figure: 7.15A). A reference datum of 450 m above sea level was selected. An extremely large initial smoothing (6000 m horizontal and 1200 m vertical) was selected to ensure stability in areas of the model with poor ray coverage (Figure: 7.16). A smoothing aspect ratio of 5:1 was chosen to allow lateral velocity variation but preserve a velocity structure that increases with depth, as low-velocity layers cannot be well constrained by this type of data. Low-velocity layers were eliminated at each iteration. The smoothing was gradually decreased to 50 m in both directions as the model converged. Larger smoothing aspect ratios resulted in very large lateral changes, and smaller aspect ratios caused low-velocity layers and a model that was streaked parallel to the ray coverage. The RMS travel-time misfit for the optimized velocity model is shown in Figure 7.17. The tomographic process stabilized quickly after three iterations.

Ray coverage (Figure: 7.16) indicates that the maximum 6-km source-receiver offsets produce refracted raypaths that penetrate no deeper than the first few hundred meters. The optimized velocity model (Figure: 7.15B) cannot be trusted below this depth of ray coverage. Deeper velocities are an artifact of the starting model and the smoothing. Based on the expected speeds of granitoids and low-grade metamorphosed basalts (*Christensen and Mooney*, 1995), the velocity model was truncated near the base of ray coverage and smoothly extrapolated with a low-velocity gradient to create a slower velocity model (Figure: 7.15C).

4.3 Seismic Reflection Processing

A ∼37 km section of the data set (vibrator points ∼13 km east and 13 km west of the boundary, along with an additional ∼12 km of receivers) was selected to be reprocessed to include steep dips (Figure: 7.5). Most of the processing was done using PROMAX Seispace (Table: 8.2). Kirchhoff prestack depth migration is used to image steep and even overturned events if turning rays are considered. This method is most useful in scenarios with complex geology, like steep dips and significant velocity contrasts.

A spherical divergence correction was applied to the data to compensate for the loss of amplitudes due to geometrical spreading using 6000 m/s. An Ormsby bandpass filter of 12-15-45-55 Hz was applied to eliminate unwanted frequencies. This filter is narrower than the vibrator sweep. The low-cut frequency reduced much of the ground roll noise, and frequencies higher than 55 Hz did not propagate several kilometers as desired for the steep-dip imaging. Dead traces, large amplitude noise from trucks, and traces near the vibrators with strong reverberation (Figure: 7.13) were deleted from the data set.

The data contain very strong surface waves (ground roll) as well as direct and refracted shear waves traveling at 3000-4000 km/s, speeds indicative of the shallow crystalline rock (Figure: 7.13). This energy remains strong and extends across the entire shot gather to the maximum 6000 m offset, which is unusual and might have resulted from the vibrators acquiring data on very thin soil over crystalline bedrock. Additionally, strong ground roll is also generated by trucks, which are infrequent but dominated by massive “road trains” from a mine along the line. Trucks and substantial back-scatter of the ground roll from modest surface topography produce strong horizontally back-scattered energy with reverse moveout. These back-scattered energy overlap with the back-scattered P-wave energy desired to image steep reflectors.

Fan filters in the frequency-wavenumber (f-k) domain were used to remove the strong and linearly coherent S-wave and surface wave noise in the gathers. The fan filters were designed to eliminate both forward and back-scattered surface and S-waves while preserving potential back-scattered P-wave energy. Apparent velocities slower than a ramp at 3800-5000 km/s were eliminated in the f-k domain. This process only partially eliminated high amplitude noise caused by the surface waves and S-waves (Figure: 7.18). Trace equalization was applied to balance trace-to-trace amplitudes after f-k filtering. A top mute was used to eliminate strong, coherent noise caused by direct and refracted P-wave arrivals.

2D Kirchhoff prestack depth migration was then applied to the data. Kirchhoff migration is a summation of diffraction hyperbolas in the time-distance domain (*Alaeil and Pajchel*, 2006). Prestack depth migration is essential to this research because it accounts for nonhyperbolic moveout caused by strong lateral variations in subsurface velocity or strong ray curvature such as required for steep dips (*Yilmaz*, 2001). This migration algorithm calculates first arrival travel times using a finite difference solution to the Eikonal equation from both the source and the receiver to every image point within a 2D gridded velocity model. Source-to-receiver times to subsurface imaging points are calculated by summing the two-way travel-time from the computed first arrival travel-times (travel-time from both source and receiver). The velocity model that was smoothly extrapolated from the travel-time tomography results (Figure: 7.15C) was used for Kirchhoff prestack depth migration. A reference datum of 450 m above sea level, above the true Earth topography, was selected to account for topographic relief along the seismic line during the migration process. The data were migrated from true topography by calculating times from the source and receiver elevations. An aperture of 36 km relative to the source-receiver midpoint and a maximum dip angle of 90 $^{\circ}$ were selected to include turning waves and vertical dips.

Several velocity models were tested to improve the prestack depth migration image results.

There were weak hints of a steeply dipping boundary when the initial velocity model (Figure: 7.15C) was used. This velocity model was changed by increments of +/- 5% for a total of four models—90%, 95%, 105%, and 110%. The results showed that reflectors in the upper ∼0.5km were more coherent and linearly consistent when using the 110% velocity model. In contrast, the lower half of the migrated data was improved when using the 90% velocity model. This suggests that velocities for the upper 100 m or more are actually faster than the tomography model, consistent with a thin weathering layer overlaying relatively unfractured bedrock. This apparent error in the velocity model is a non-uniqueness artifact of the 50 m gridding and smoothing in the tomography and a thin (likely <10 m) weathered layer. Tomography smeared the low-velocity weathered rocks into the upper 100 m or more and compensated by slightly increasing the deeper velocity.

Based on the above observation, two additional velocity models were created. In both velocity models, the wave speed in the shallower portion was increased by 10% of the tomography model, and the wave speed in the deeper sections was decreased by 10% of the extrapolated tomography model. In the first model, the velocity gradient rapidly changes from the shallow to the deeper section. In the second model, velocity gradually decreases from the shallow to the deeper section. Three iterations of tomography were applied to these velocity models to ensure that the models still matched the first arrival times, did not have low-velocity zones, and the velocity gradient was smooth. The best results from the migration were for the faster gradient velocity model where the starting velocity for the upper ∼ 50 m was >4300 km/s, and the change in velocity gradient decreases rapidly once depths of ∼200 m below sea level are reached (Figure: 7.19A).

Chapter 5

Interpretation and Discussion

The Mount Edgar dome in the western half of the study area is composed of granitic (TTG) rocks, dominated by the Cleland and Emu Pool supersuites and their low-grade metamorphosed equivalents (Figure: 7.6). The greenstone unit adjacent to the dome near the seismic line is the Warrawoona Group composed of very low-grade metamorphosed mafic volcanics and lesser ultramafic volcanics. The Fortescue Group overlies the Warrawoona greenstones, and is dominated by mafic volcanic rocks and includes felsic lava flows and sedimentary rocks (*Williams and Hickman*, 2007). Crystalline bedrock is well exposed, the soils are thin in a desert climate, and the only sediment deposition is in broad, shallow river channels (Figure: 7.5).

The simple 1D velocity analysis (Figure 7.14), the 2D tomography velocity model (Figure 7.19C), and the velocity model improvements suggested by the migration velocity analysis (Figure 7.19B) all indicate a very thin weathered layer over bedrock along the entire study portion of the seismic line. While these models were limited in resolution by the geophone station spacing and 2D velocity model gridding, all indicate that weathered rocks are much less than 50 m thick; they are likely mostly <10 m thick. The seismic velocity increases very rapidly from <4000 to >4500 m/s in the upper ∼50 m, representing the under-sampled soil and the underlying bedrock speeds. Velocity continues to increase rapidly to >5500 m/s at 200-500 m depth, interpreted to be due to exhumation and weathering fractures that close with depth. The velocity gradient rapidly decreases to an almost constant value at

200-300 m below the surface in the granitoids and ∼500 m in the Fortescue. The refraction analysis only constrains the velocity to these very shallow depths at which the velocity gradient becomes very small (Figure 7.12A). The weaker constraints from migration velocity analysis suggest that velocity does not significantly increase beneath the base of refraction ray coverage (Figure 7.19). The average compressional wave velocity at 5 km depth in granitic rocks is ∼6100 m/s, and low to medium-grade metamorphosed basalt is ∼6300-6650 m/s (*Christensen and Mooney*, 1995). The velocity reaches unfractured bedrock speeds at a few hundred meters depth in the granitic dome, but the velocity is slower in the Fortescue half of the line. Young basalts usually have much slower velocity than unfractured basalt due to pervasive fracturing. The basalts of the Fortescue are very weakly metamorphosed and may still contain volcanic fracturing. In addition, volcaniclastic sediments and local felsic volcanic rocks (Figure 7.6) may have decreased the local shallow velocity.

The Kirchhoff prestack migrated image (Figure 7.20) in the Mount Edgar dome in the western half of the line shows weak but coherent reflectors at shallow depths that fade within the first ∼1 km. This weak reflectivity is interpreted to be due to exhumation fracturing or to minor internal boundaries within the fairly uniform granitic rock. Fracturing closes rapidly with depth, and the seismic signal decays with depth. The underlying crust contains no reflectivity to the 4 km depth imaged here and to >15 km depth in previous processing (*Doublier et al.*, 2020). This is interpreted to represent the minimum vertical extent of the Mount Edgar dome granitic complex.

The east side of the migrated image (Figure 7.20) is within the mafic volcanics of the Fortescue basin. The bottom of the Fortescue basin and presumed top of older greenstones produces high amplitude reflectors that slope westward from ∼2 km to ∼3.5 km in depth approaching the edge of the Mount Edgar dome. Shorter strong reflectors within the Fortescue represent its sub-horizontal, layered volcanic, and sedimentary rocks. There are also small faults

within the Fortescue basin and at its base. This boundary is regionally depositional, and there has been only minor younger deformation, so the structure on this reflector is interpreted to represent the paleo-surface prior to deposition and minor faulting associated with extrusion. Like in the previous seismic processing (*Doublier et al.*, 2020), no reflectivity is observed within the greenstone units that underlie the Fortescue Group.

While there is geological evidence of a steeply dipping boundary of the Mount Edgar dome to the north and south of the seismic line (Figure 7.5), at the exact location where the line crosses the boundary, the geologic maps show a more complex relationship (Figure 7.6). The state geologic map (*Williams and Hickman*, 2007) indicates a very crooked granitoid-greenstone boundary at the surface and minor faulting that cross-cuts the boundary. The inferred location of the granite-greenstone boundary is an approximately 2-3 km section of the migrated image (Figure 7.20). There are several dipping reflectors in the area; however, similar reflections cross each other in opposite directions. The westward-dipping reflections are created by shots to the west, while the eastward-dipping reflections are from shots to the east. This suggests a velocity model error, but no reasonable change in velocity can reconcile these reflections to be from the same boundaries. They are perhaps not migrating correctly due to the 3D nature of the geology (Figure: 7.5) as well as the crookedness of the seismic line in the area (Figure: 7.6). A crooked or oblique line can result in imaging an apparently less steep dip as the reflection points are not in a vertical plane. 3D geology can result in an incorrect 2D image, including conflicting dips. While, in theory, a crooked line can be used to image portions of a 3D structure through 3D migration, this seems unlikely to succeed given the relatively weak reflectivity and poor constraints on 3D velocity. These intriguing features are interpreted to be real reflections from steep boundaries, but unfortunately, the data cannot reveal their accurate geometry.

The very weak seismic velocity gradient after a few hundred meters of depth limits the

maximum depth to which reflections can be imaged (Figure: 7.12A). Longer offsets were included using sources and receivers, both far from the boundary (but within 6 km of each other). Still, the migrated data do not sample vertical boundaries greater than ∼1.2 km subsurface depth. Therefore, even if the 3D and crooked line issues can be eliminated with a better survey, the maximum depth at which the boundary could be observed would be limited to the upper few kilometers by the methods used here.

Other features in the migrated image (Figure 7.20) reach very steep dips; however, they are not linearly coherent and either lose energy or are truncated by other more dominating features in the data as depth increases. They have a different character than the reflections within the boundary zone, resembling migration "smiles" from a noise impulse in the pre-migrated data. All these steep features lie at Earth's surface or the edges of the migrated image and are interpreted to be artifacts caused by migration. A few steeply dipping structures beneath the Fortescue Group could be interpreted as vertical reflections within the underlying greenstones; however, these resemble migration artifacts observed at the ends of the line and are likely not real reflectors.

The Kidson seismic survey was a multichannel deep crustal survey designed for regional exploration purposes. It was not explicitly designed to show the steeply dipping features of the Pilbara Craton; in fact, the Pilbara portion of the line was an inexpensive add-on to the main survey. There is substantial noise in the data caused by both S-waves and surface waves (Figure: 7.13). The strength of these waves is unusual and is related to the very thin soil over crystalline bedrock. Improved vibrator arrays and/or geophone group arrays may reduce this strong noise.

The research can be further improved if 3D wide-angle seismic reflection data were acquired at a location where the greenstones are exposed to the surface and the boundary is linear and well-defined. Much of the geologic work has been performed at such boundaries. Perhaps the

best example is the exposed granitoid-greenstone contact southwest of the Mt. Edgar dome near the town of Marble Bar. Such a dataset could image at depth the vertical greenstones as well as the boundary between the granitic complex and the circumjacent greenstones. A good velocity model with a larger spatial aperture than what was recorded by this multichannel deep crustal survey would improve the migration imaging. One limiting factor that would be difficult to overcome would be the maximum depth of turning waves, and hence the maximum depth of reflected turning waves, caused by the low-velocity gradient within the crystalline rocks.

Chapter 6

Conclusion

Kirchhoff prestack depth migration of the data acquired by the EFTF program along a 37 km section of the Kidson seismic line images a poorly reflective granitic dome that extends much more than 4 km into the subsurface to the west and 2-3 km of layered volcanic flows overlaying greenstones to the east. These features are consistent with previous imaging. Seismic velocity models indicates that the weathered zone is <10 m thick overlying fractured crystalline rock, and that the fractures close within a few hundred meters of the surface. Seismic velocities in the granitic dome are consistent with granitic rocks. Velocities in the Fortescue Group are somewhat slower than expected for mafic volcanic rocks, suggesting volcanic fracturing and/or more felsic volcanic and sedimentary rocks. The new migrated seismic reflection image was processed to include steep dips, and shows multiple features dipping $\sim$45-55° in both directions at the granitoid-greenstone boundary. These structures suggest incomplete imaging, which could be due to errors in the velocity model, the 3D nature of the mapped local geology, and/or the crooked 2D seismic line. These indications of steep reflectivity are consistent with the steep geologic structures observed at the surface, but do not definitively constrain the structures at depth. It is not possible with these data to narrow the tectonic mode by which the Mt. Edgar dome and the Pilbara Craton were modified.

Chapter 7

Figures

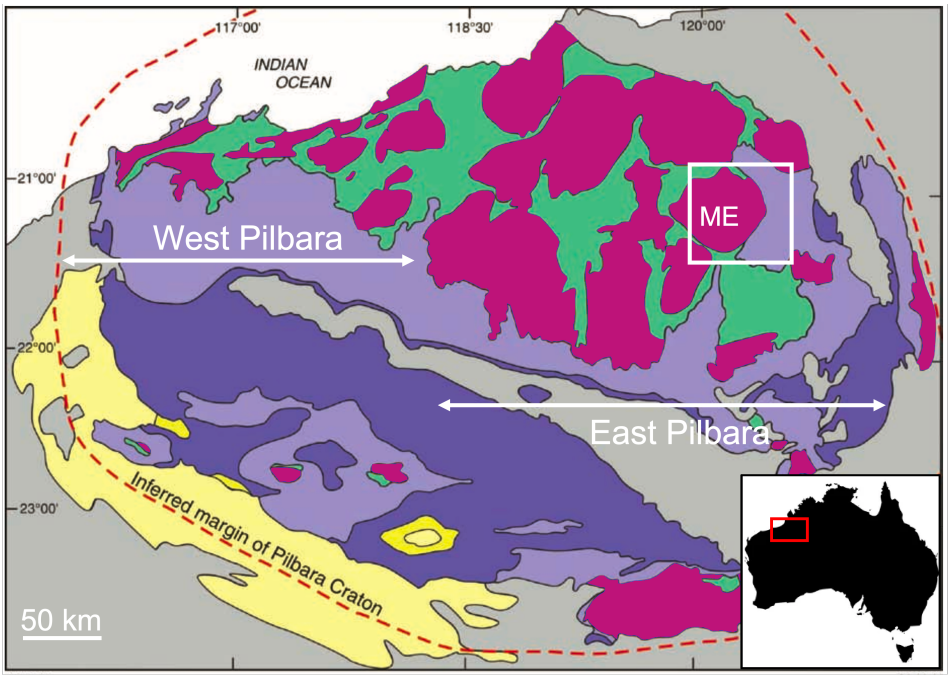

Figure 7.1: Geology map of Pilbara Craton. The inferred margin of the Pilbara Craton is shown with a dashed red line. Green indicates greenstone belts and pink indicates the granitic domes. The study area and Mount Edgar dome (ME) is highlighted with a white box. The purples show the 2.7 Ga Fortescue Group, Hamersley flood basalts, and yellow and gray are younger sedimentary rocks and sediment. The inset map on the lower right corner shows the location of the Pilbara Craton in Western Australia show in a red box. (from *Hickman and Van Kranendonk*, 2012[1])

[1]Permission for use of figure in Appendix B

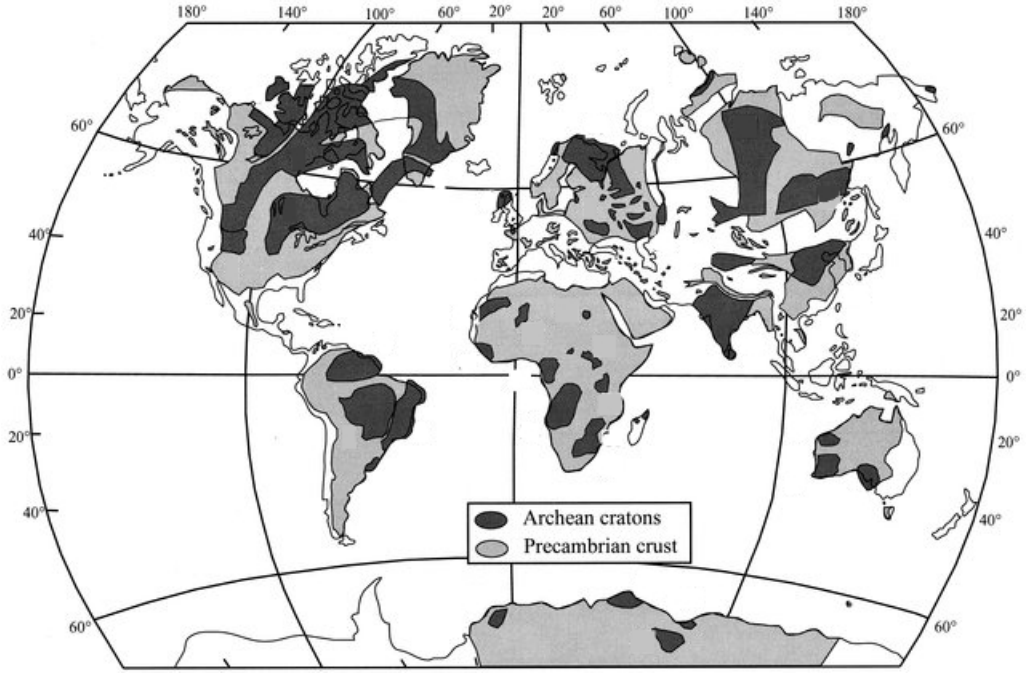

Figure 7.2: Global distribution of Archean cratons (dark grey) and Precambrian crust (light grey) (from *Kusky and Polat*, 1999[1])

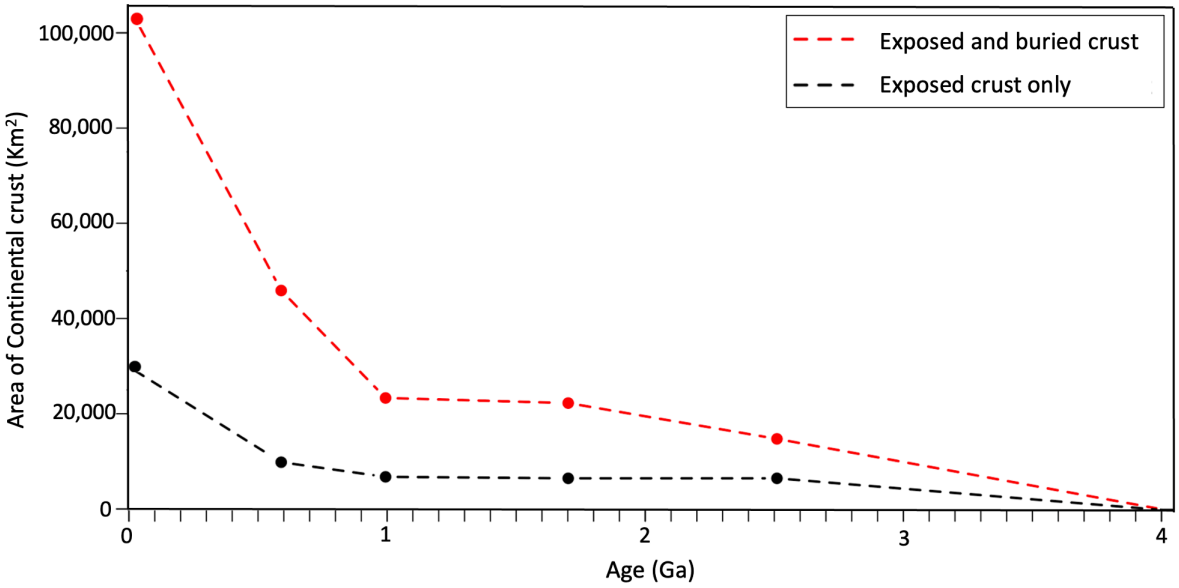

Figure 7.3: Distribution of geological ages in presently preserved crust (data from *Goodwin*, 1996). The black dashed line indicates the surface area of crust that is exposed at the surface. The red dashed line indicates the total surface area of crust that is exposed and buried underneath younger rocks.

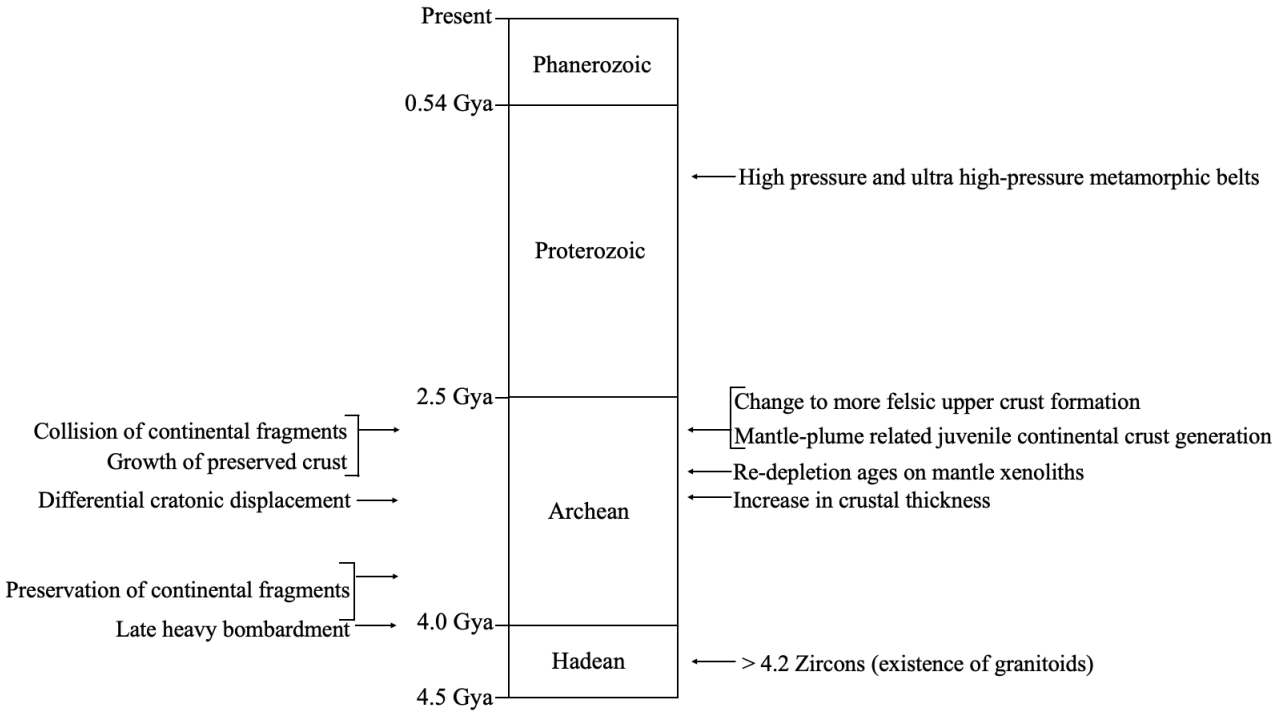

Figure 7.4: Geologic timescale and major events in Earth's history as related to plate tectonics. Chronologically, from oldest to youngest: earliest zircons from Jack Hill (*Harrison*, 2009; *Hopkins et al.*, 2008, 2010) date back to 4.2 Ga, late heavy meteorite bombardment (4.0 Ga to 3.85 Ga) (*Harrison*, 2009), preservation of earliest continental fragments began by 3.8 Ga (*Goodwin*, 1996), crustal thickness started increasing by 3.1 Ga (*Dhuime et al.*, 2012), evidence of differential cratonic displacement in reliable paleomagnetic data starting at 3.1 Ga (*Cawood et al.*, 2006), geochemical signature of melts suggest depletion of mantle started by approximately 3.0 Ga (*Hawkesworth et al.*, 2017), global evidence for crustal growth and structural evidence for horizontal shortening commence by 2.9 Ga (*Van Kranendonk et al.*, 2007; *Smithies et al.*, 2007; *Hickman and Van Kranendonk*, 2004), 2.7 Ga marked the change to more average felsic upper crust (*Tang et al.*, 2016) as well as the generation of mantle plume related juvenile continental crust generation(*Condie*, 2005), and 1 Ga marks the presence of blue-schist and ultrahigh pressure metamorphism (*Stern*, 2005; *Brown*, 2006; *Brown et al.*, 2020).

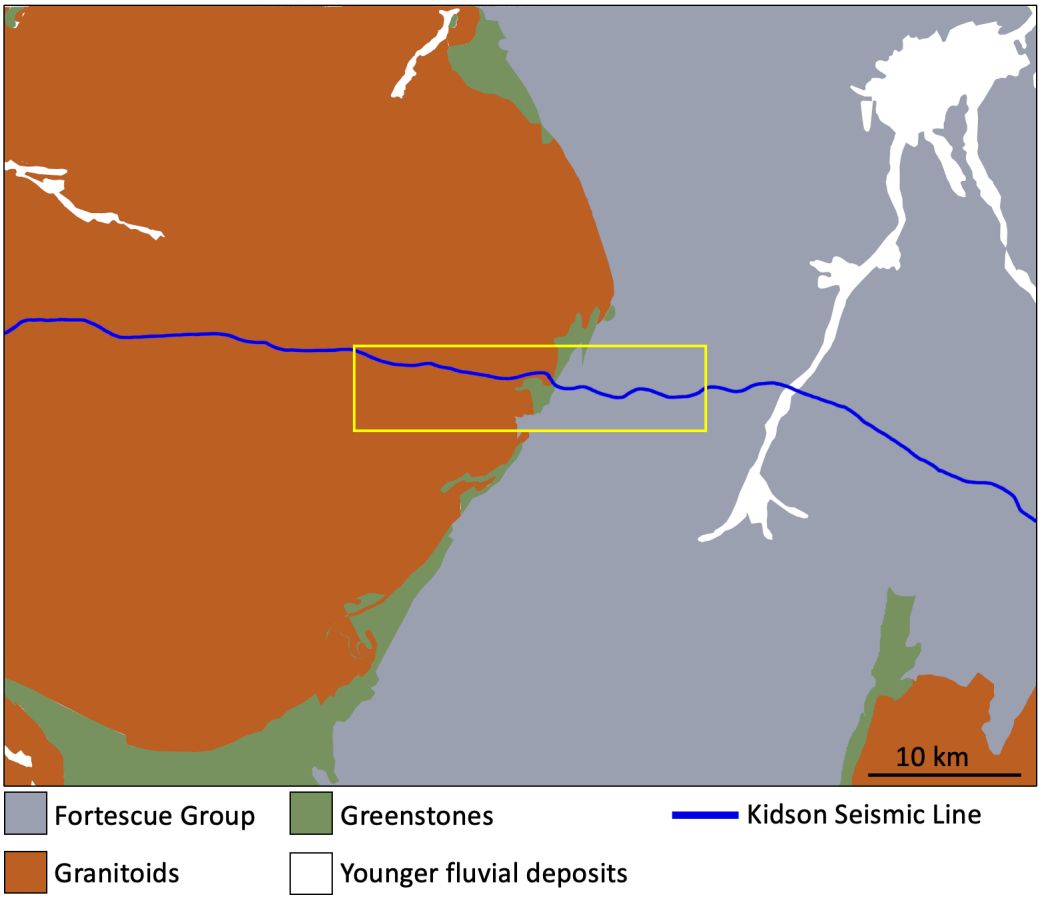

Figure 7.5: Geology map of Mount Edgar dome. Map shows the distribution of TTG granitoids (orange), greenstones (green), along with overlying Fortescue (grey), and younger fluvial deposits (white). The Kidson seismic line is blue. The yellow box shows section of the seismic data that will be reprocessed (Figure: 7.6). Modified from map by *Williams and Hickman*, 2007.

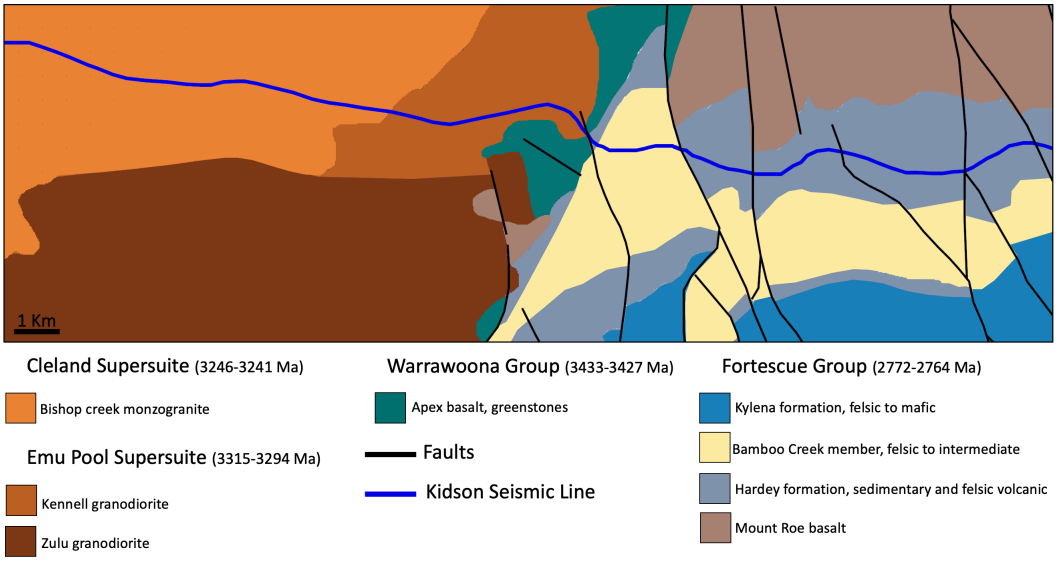

Figure 7.6: Detailed map of the granitoid-greenstone boundary. This map shows the section of the seismic line that is being reprocessed (yellow box in Figure 7.5). The granitoids of the Mount Edgar dome on the left consists of the Emu Pool supersuite formations ranging from 3315 to 3294 Ma (rust and dark brown) and the Bishop Creek formation (3246-3241 Ma) from the Cleland supersuite (orange). The Warrawoona Group consists of greenstones deposited around 3433-3427 Ma (green). The Fortescue group consists of Mount Roe basalt (brown) that underlies the sedimentary and felsic volcanic rocks of the Hardey formation (grey). The Bamboo Creek volcanics member(yellow) is rhyodacite lava that is a part of the Hardey formation. The felsic to mafic volcanics of the Kylena formation (blue) overlay the Hardey formation. Proposed faults in the area are shown in black and the seismic line is shown in blue. Modified from map by *Williams and Hickman*, 2007.

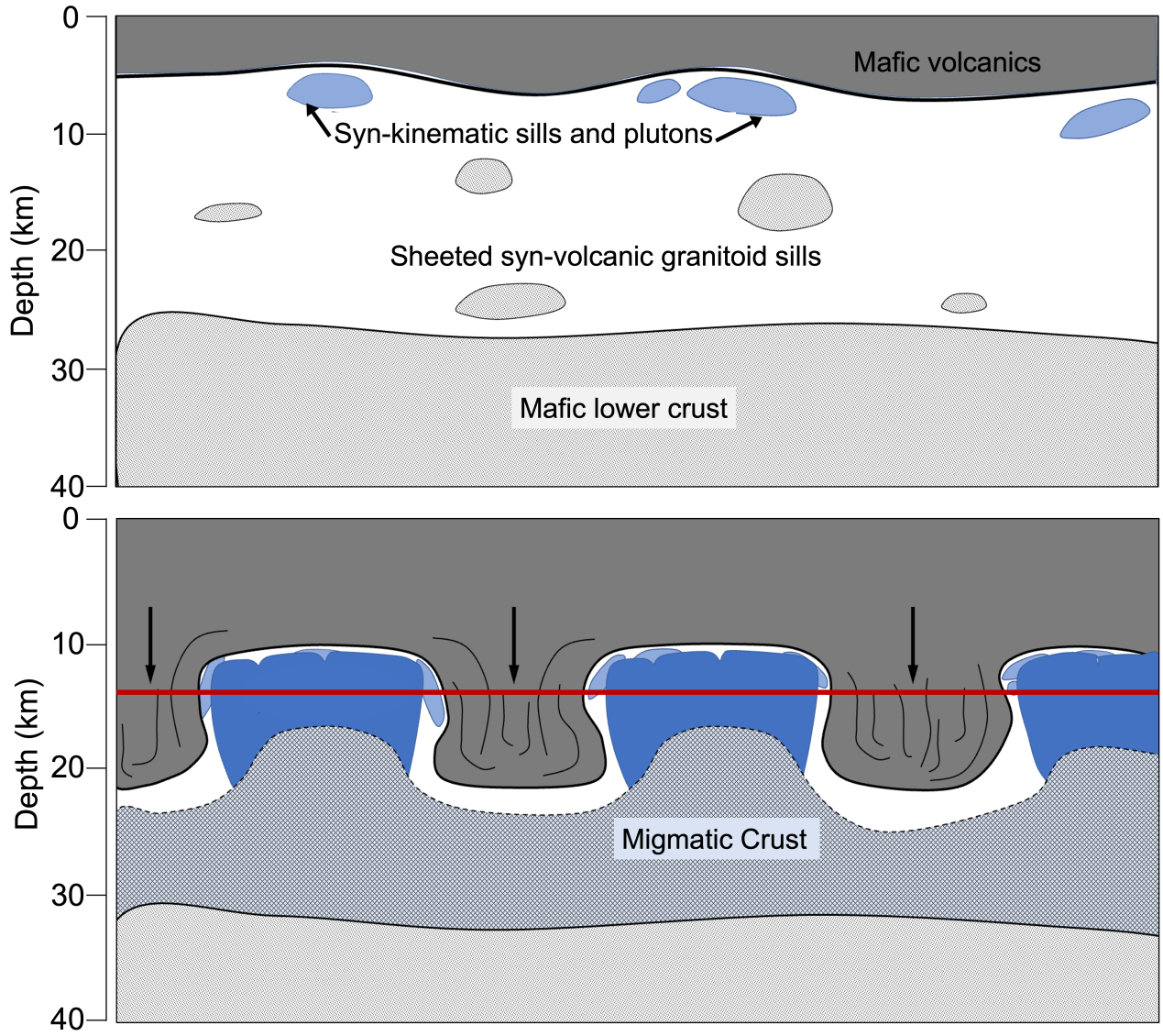

Figure 7.7: Proposed partial convective overture model showing buoyancy driven processes that could have formed dome and keel structures (*Collins and Van Kranendonk*, 1989). Mafic flood basalts are deposited on preexisting crust that includes granitoids (TTG). The presence of denser material on top of less dense granitoids in a hot crust environment causes the granitoids to diapir upward in the solid state and greenstones to "sagduct" downward. This makes the greenstone lava flows vertical and circumjacent to the granitic dome complex. Red line portrays the present-day surface of the dome and keel structures. Figures adapted from *Roberts et al.*, 2022.

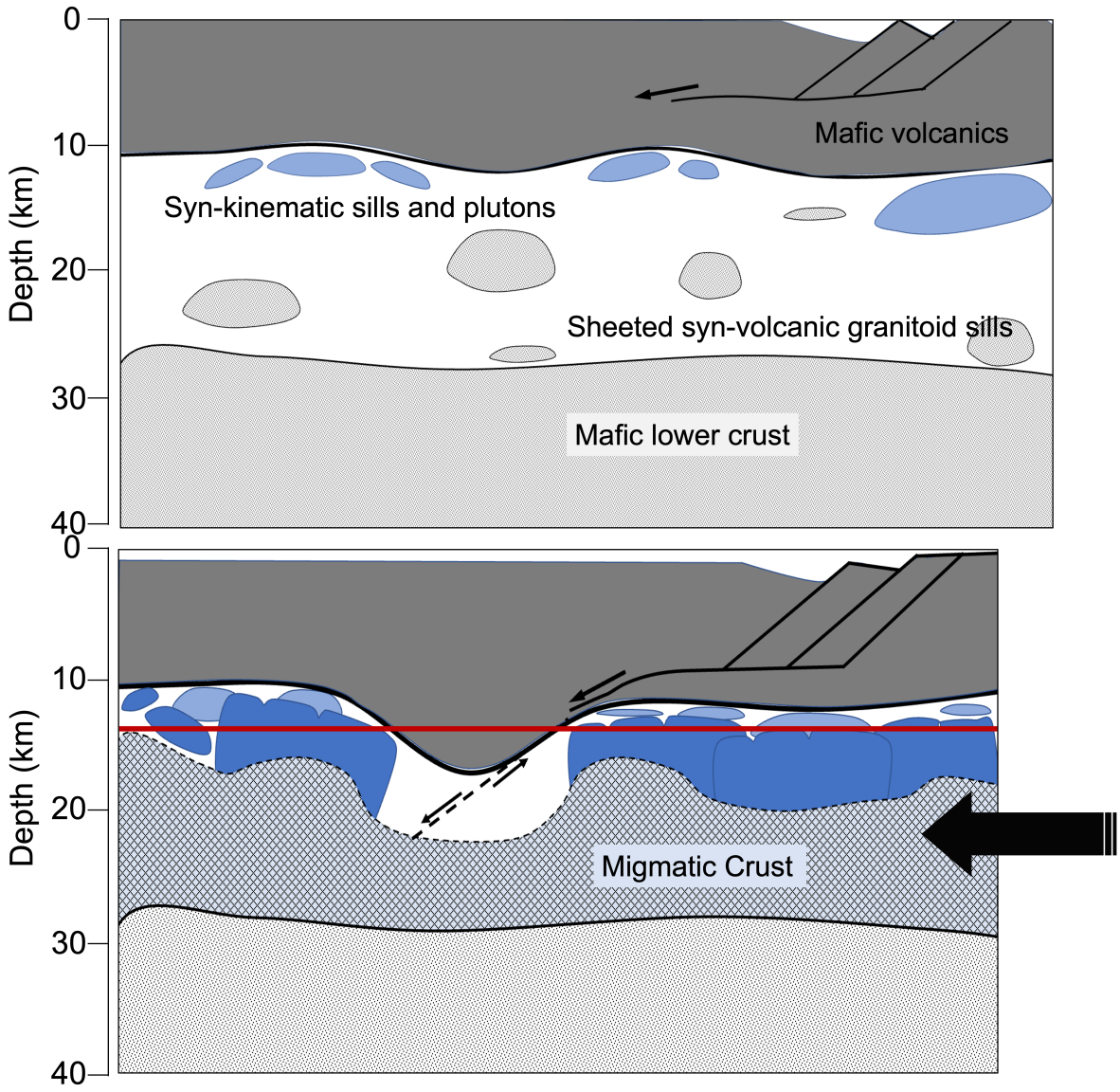

Figure 7.8: Extensional core-complex model showing horizontal proto-plate tectonic processes that could have formed dome and keel structures through sequences of horizontal contraction followed by extension (*Kloppenburg et al.*, 2001). Black arrow indicates concurrent or younger compressional deformation perpendicular to the figure. Red line portrays the present-day surface of the dome and keel structures. Figures adapted from *Roberts et al.*, 2022.

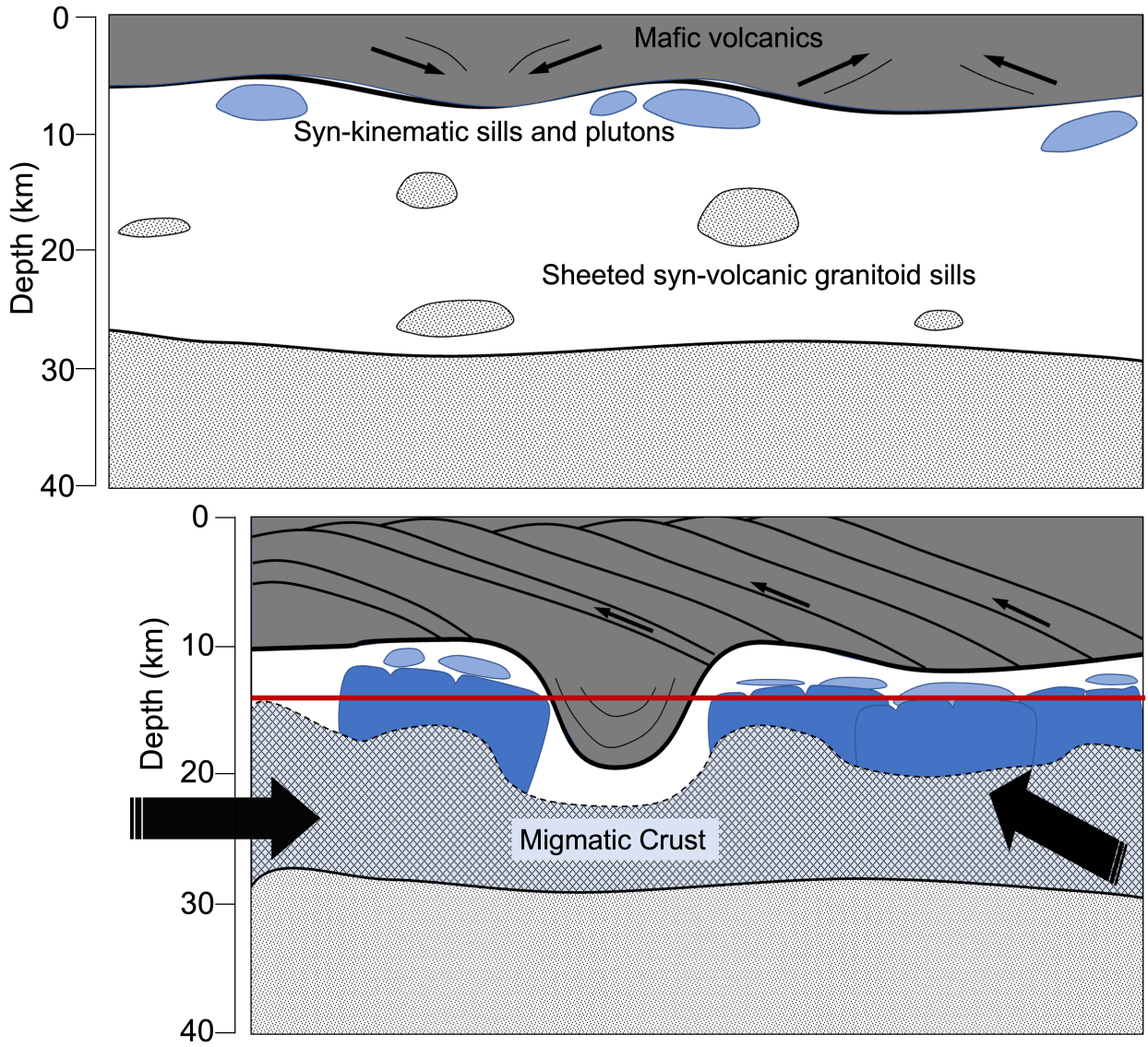

Figure 7.9: The fold interference model also showing horizontal proto-plate tectonics processes that could have formed dome and keel structures due to horizontal buckling of the crust in multiple directions (*Blewett*, 2002). Figures adapted from *Roberts et al.*, 2022.

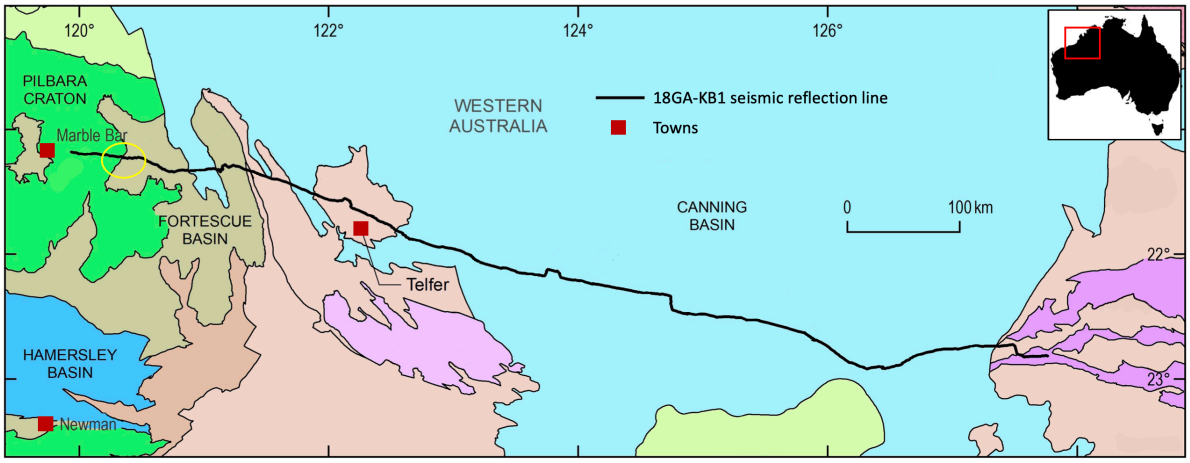

Figure 7.10: Map of Kidson seismic reflection line acquired by EFTF (from *Doublier et al.*, 2020[1]). The 872 km line extends across Proterozoic orogens (pink and light brown) and the overlying Phanerozoic Canning Basin (blue, light green) and into the Pilbara craton (green) on the west. Area is interest is marked by a yellow circle.

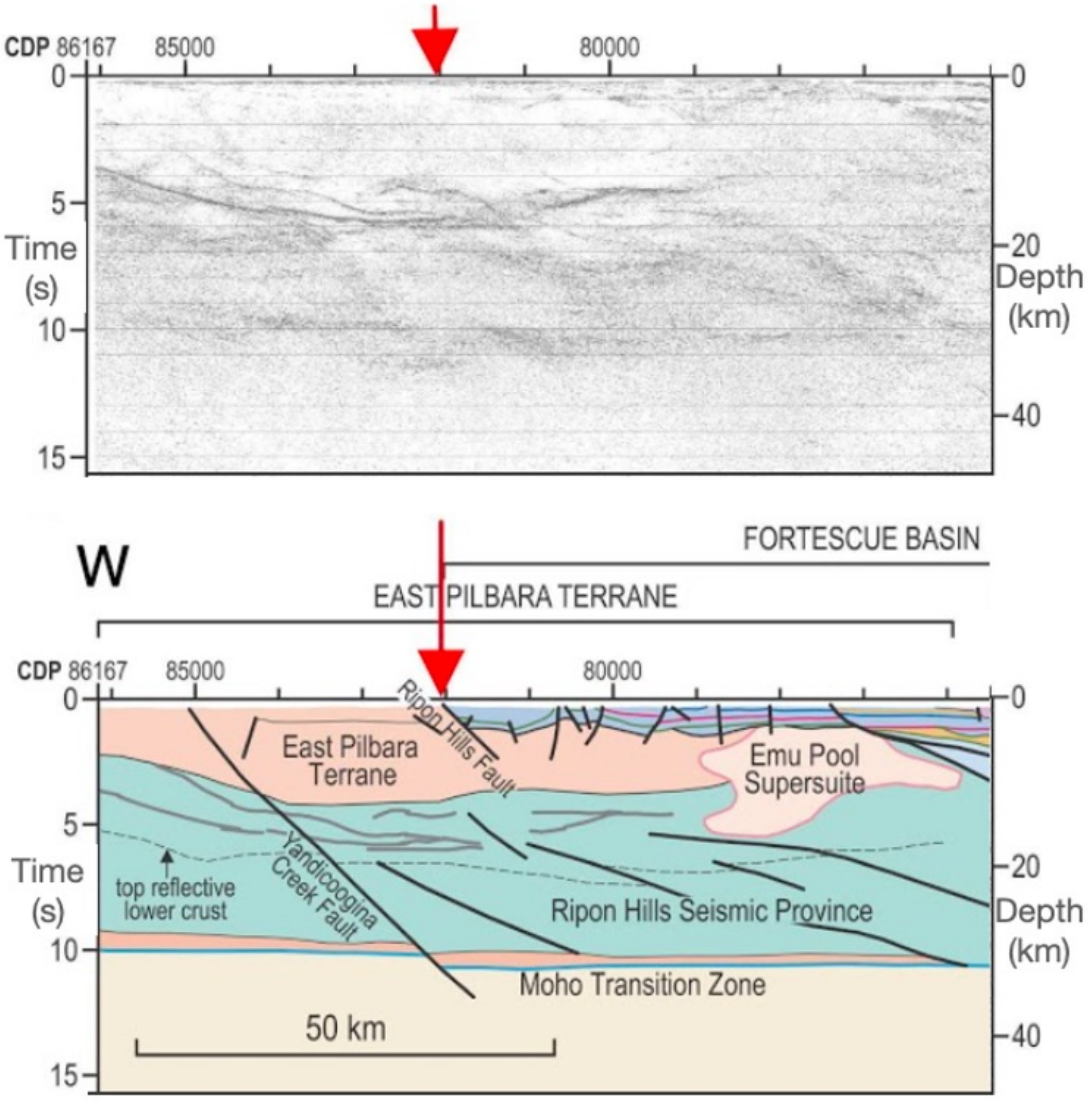

Figure 7.11: Processed and interpreted seismic data of the East Pilbara terrane portion of the Kidson seismic line (from *Doublier et al.*, 2020[1]). TOP: migrated seismic reflection section. BOTTOM: Geological interpretation. Y axis represents two-way travel time (s) on the left and approximate depth (km) on the right assuming a velocity of 6000 m/s. Red arrow indicates the approximate location of the granitoid- greenstone boundary. Vertical exaggeration is 1:1.

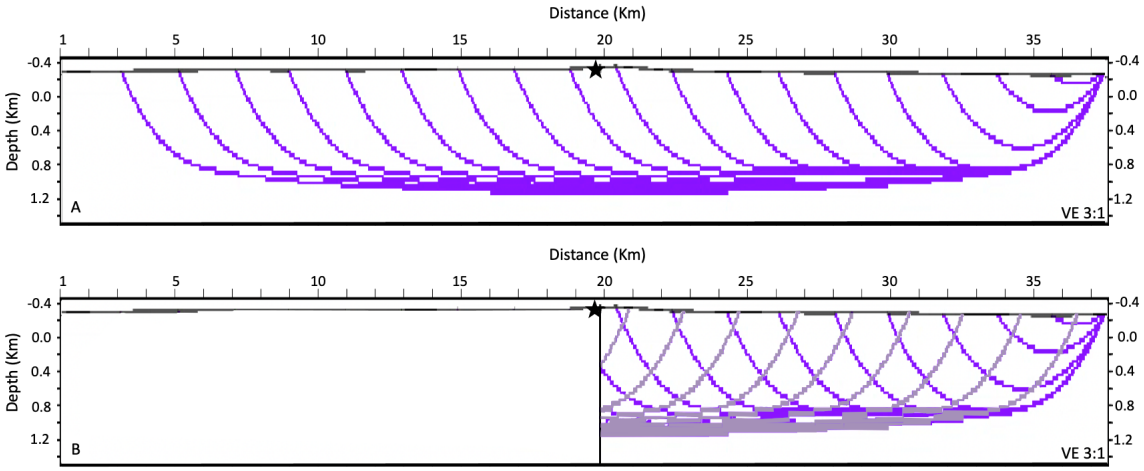

Figure 7.12: A) Ray paths for a single shot through the velocity model of Figure 7.19B. Refracted turning waves (purple) can constrain velocity to ∼1.0-1.5 km subsurface. B) turning rays reflected (grey) off a steeply dipping boundary at the approximate location of the granitoid-greenstone boundary (star). Sea level is at 0 km depth. Vertical exaggeration is ∼3:1.

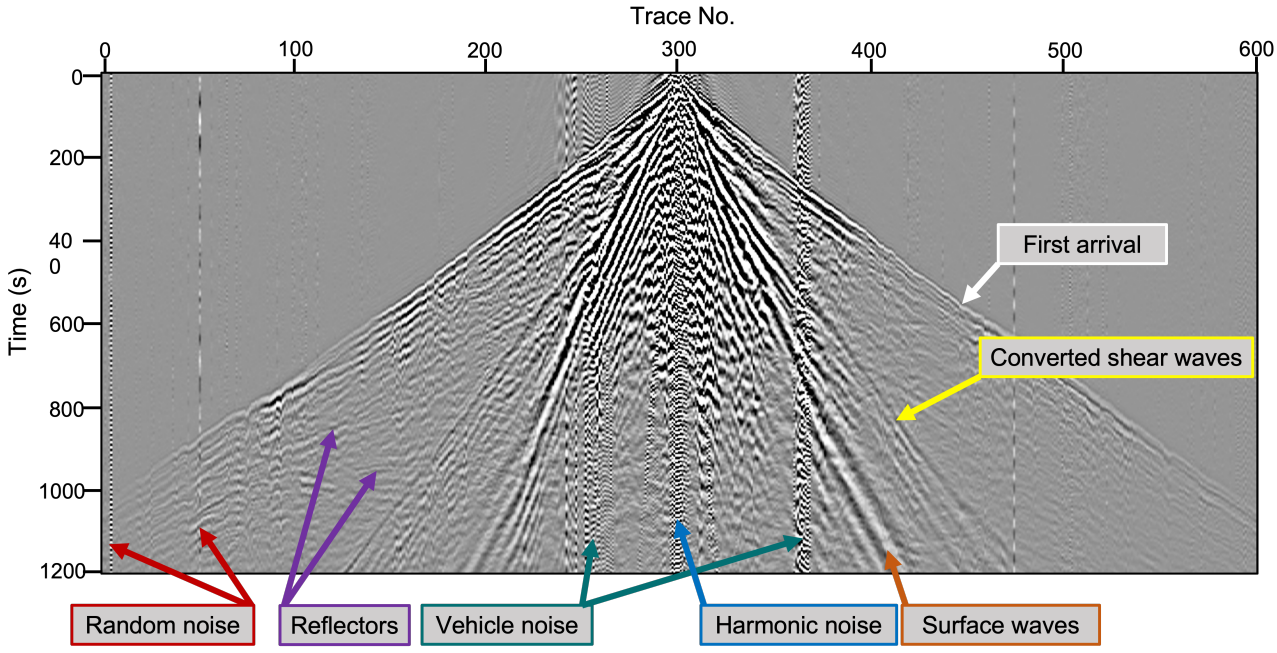

Figure 7.13: Raw vibrator point gather located ∼ 10 km east of the granitoid-greenstone boundary. Spherical divergence has been applied. There were 600 receiver stations per vibe point, centered at the vibe point. First arrivals have a p-wave velocity of 6000m/s. Shear waves have a velocity of 3500 m/s. Surface waves are in orange. Noise includes random bad traces, vehicle noise, and harmonic shaking near the vibe point.

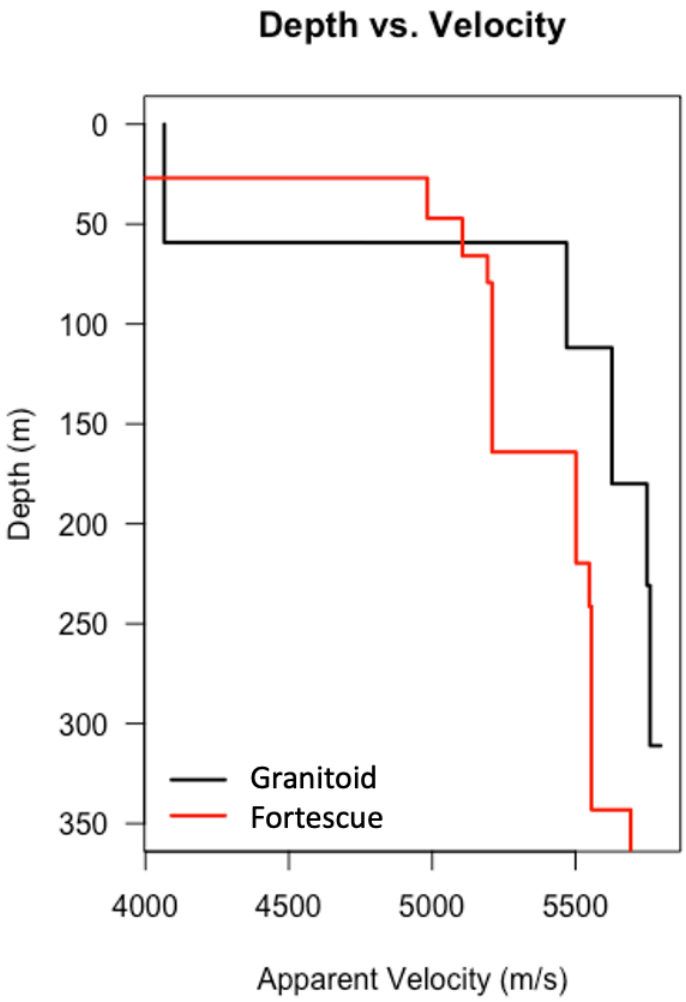

Figure 7.14: 1D velocity models derived from first arrival travel-time picks. Velocity of granitoids (black) rapidly increases to bedrocks speeds within 50 m depth. Velocity of Fortescue flood basalts (red) gradually increases within the first 350 m.

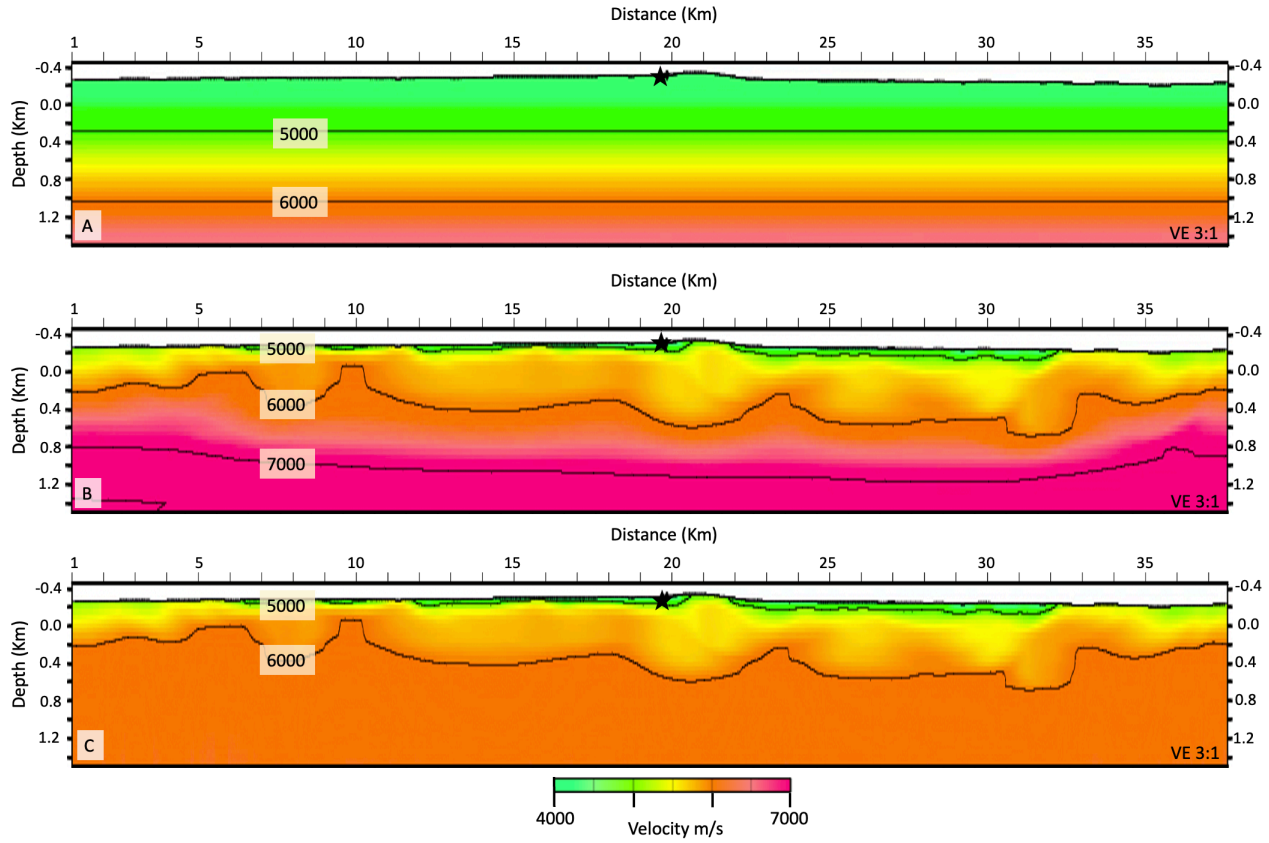

Figure 7.15: Velocity models for travel-time tomography. A) starting model for the inversion. B) Final model after 24 iterations. C) Velocity model deleted below ray coverage (Figure 7.16) and extrapolated with a lower velocity gradient. Velocity in the final iteration reaches speeds of more than 5500 m/s within 0.2 – 0.4 km below surface. The approximate location of the granitoid-greenstone boundary is denoted by a black star. Sea level is at 0 km depth. Sea level is at 0 km depth. Vertical exaggeration is ∼ 3:1.

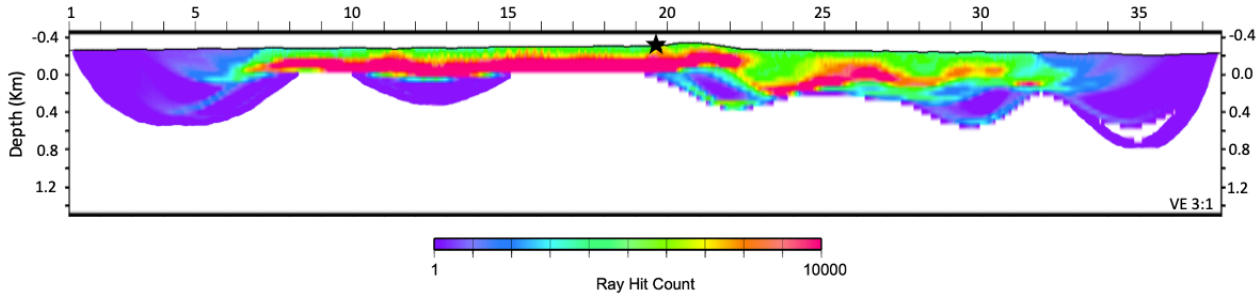

Figure 7.16: Ray tracing through through the velocity model of Figure 7.19B. Hit counts are in 50-m grid cells for rays for all seismic traces with picked first arrival travel times. The approximate location of the granitoid-greenstone boundary is denoted by a black star. Sea level is at 0 km depth. Vertical exaggeration is ∼3:1.

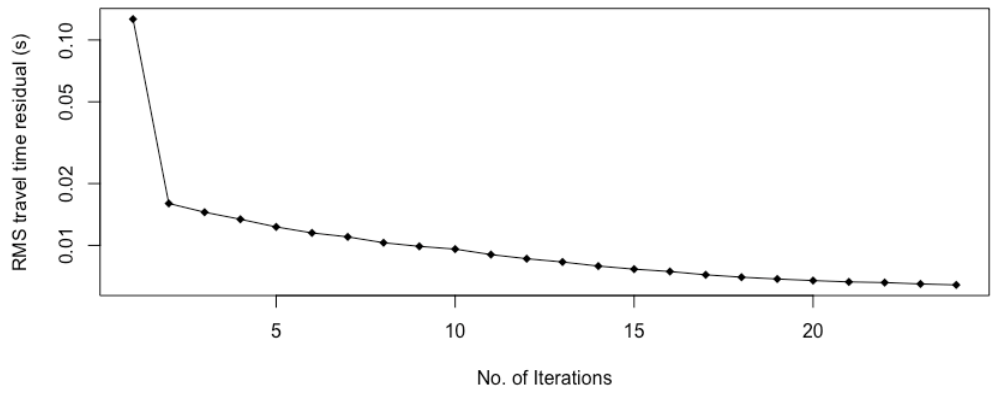

Figure 7.17: RMS travel time residual for velocity model shown in Figure 7.15B as a function of iteration number.

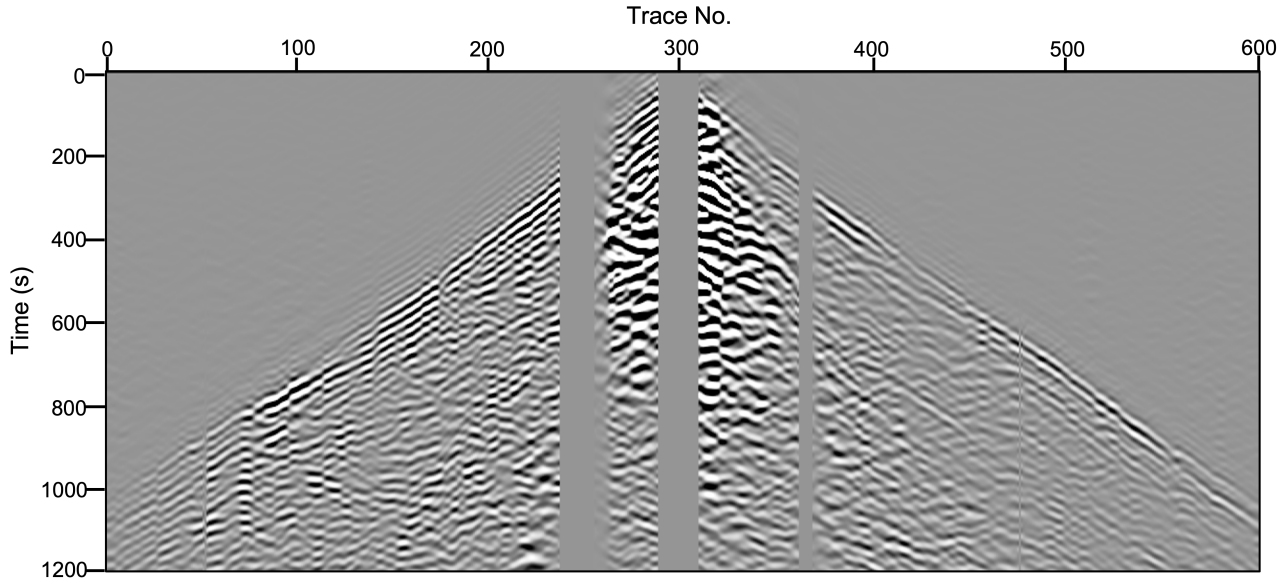

Figure 7.18: Vibrator point gather of Figure 7.13 with noise removed. Bad and noisy traces have been removed and a f-k filter was used to reduce strong, slow shear-wave and surface-wave noise. There is still remaining noise from the shear and surface waves.

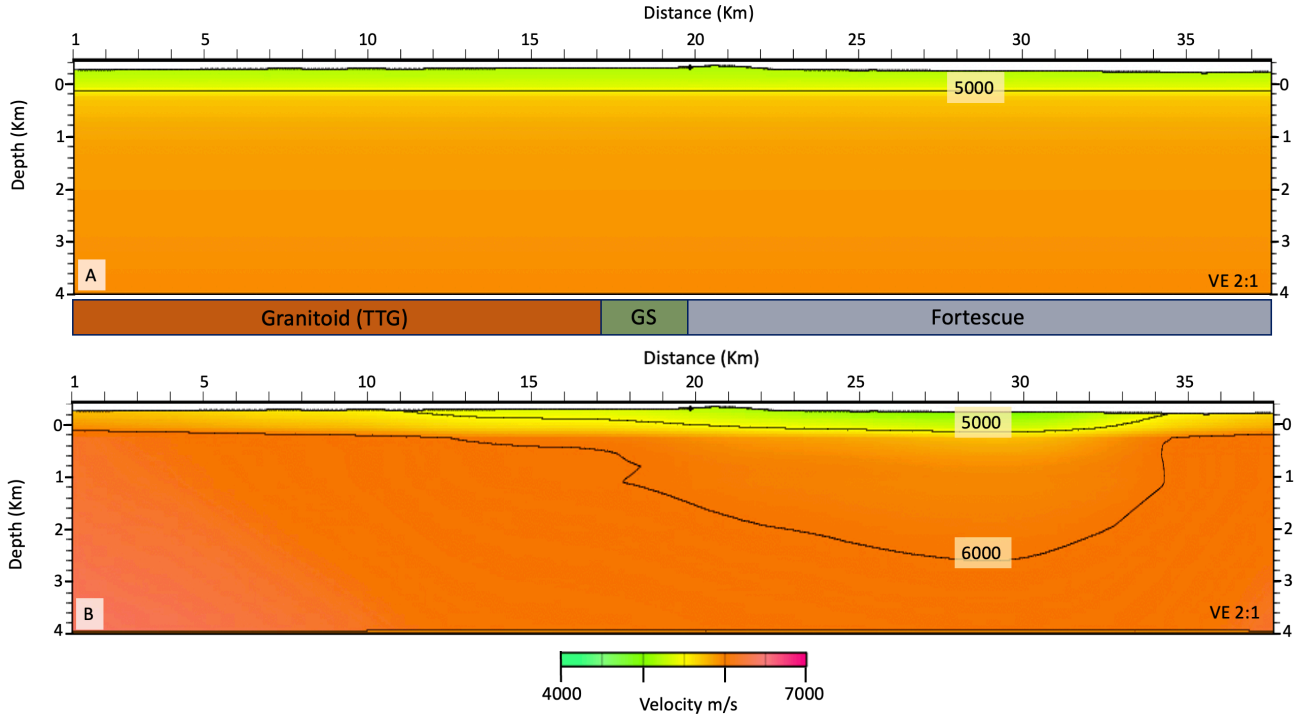

Figure 7.19: Final velocity model used for Kirchhoff prestack depth migration. A) starting model. B) Velocity model after 3 iterations of travel time tomography. Velocity in the final iteration reaches speeds of more than 5500 m/s within 0.2–0.4 km below surface. The right side of the plot where velocity increases gradually to 6000 m/s is within the Fortescue Group. The zone of steeply dipping greenstones (GS) is approximately 3 km wide in the center of the model. The velocity rapidly reaches 6000 m/s in the granitic complex. Sea level is at 0 km depth. Vertical exaggeration is ∼2:1.

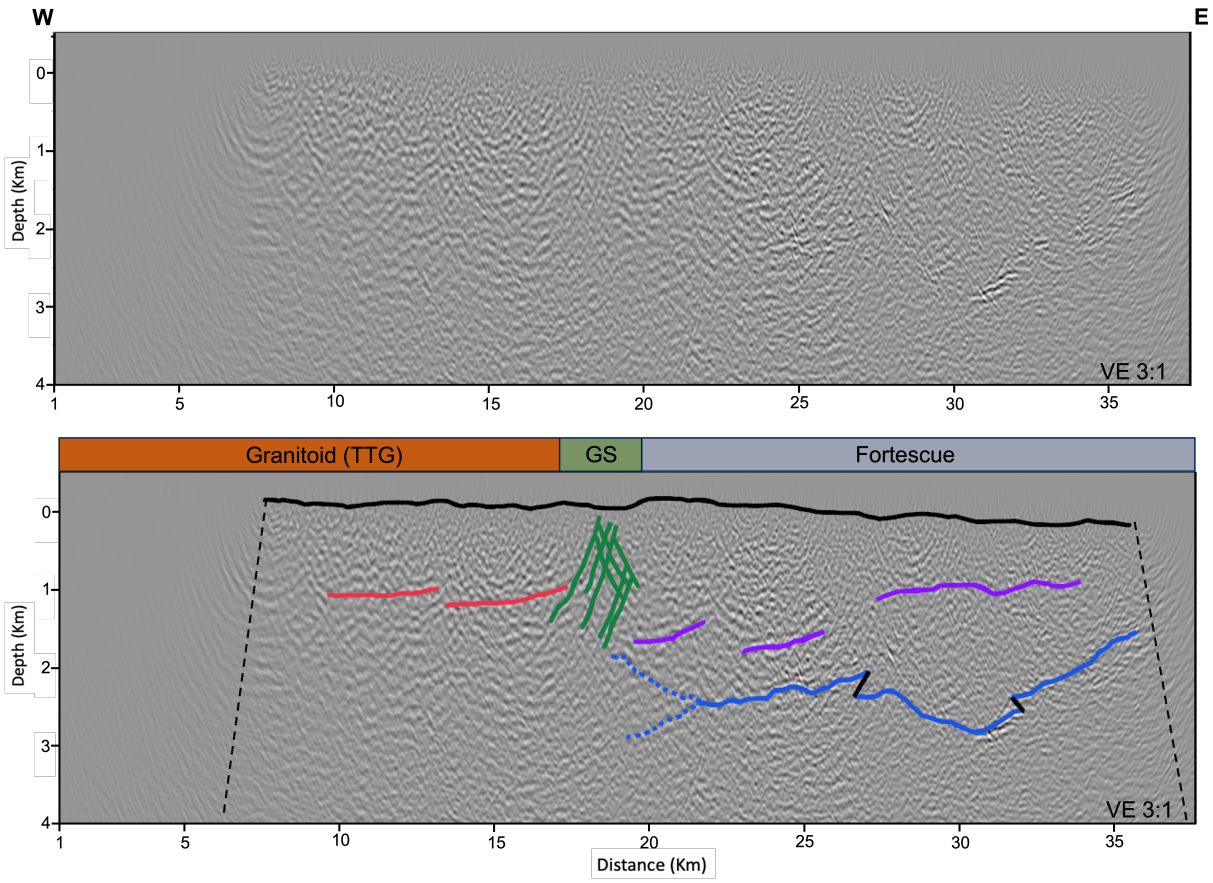

Figure 7.20: Migrated seismic section. Top: Uninterpreted. Bottom: Interpreted. Granitoids are on the left, ∼3 km-wide zone of the steeply dipping boundary in the middle, and Fortescue Group is on the right. Solid black line refers to the land surface. Dashed black line marks the extent of the migrated image without any migration artifacts due to lack of vibrator points along the edges. Dashed red line marks the approximate depth of weak reflectors in the granitoids. Green line shows cross-cutting reflectors dipping in both directions within the ∼3 km range of the granitoid-greenstone boundary. Yellow line shows other examples of steep reflectors in the migrated section. Reflectors from Fortescue are sharply truncated at the right most green line. Reflections interpreted as the bottom of formations within the Fortescue Group are shown in purple. Reflections interpreted as the bottom of the Fortescue group are shown in blue, with minor faults. Dashed blue shows two possible directions in which the base of the Fortescue group can be interpreted. Sea level is at 0 km depth. Vertical exaggeration is ∼3:1.

Chapter 8

Tables

Parameter	Value
2D line direction	east-west
System Type	Sercel 428 XL
Sampling interval	2 ms
Record length	20 s
Filters	0.8 Nyquist, 200 Hz, linear
Geophone	SM24 10 Hz
Receiver	groups of 6 geophones, 3.33 m spacing
Group interval	20 m
Receiver array location	centered on stations
Nominal fold	150
Channels	600
Spread	12 km (symmetrically split)
Source type	Vibrator trucks: Inova AHV-IIV PLS-364 62 000 lb
Source pad to pad	12 m
Source array length	24 m
Vibrator intervals	40 m
Vibrator array location	center of spread
Sweep length	24 s
Sweep type	linear upsweep
Sweep frequency	4-96 Hz
Sweep drive levels	75 % nominal

Table 8.1: Seismic acquisition parameters for 2018 seismic survey of the Kidson Sub-basin (*Carr et al.*, 2022).

SEG-Y to Disk import
2D Land Geometry Assignment
First Break picks
Velocity analysis: Travel-time tomography
Noise Attenuation
Bandpass filter
F-k Fan filter
Trace kill: narrow offset noise
Trace kill: trucks
Trace equalization
F-k Fan filter
Trace muting:top mute
Migration
Common Offset Gather Binning
Velocity model export
Kirchhoff Depth Migration
Velocity Model analysis
CDP ensemble stack

Table 8.2: Seismic processing steps

Bibliography

Alaeil, B., and J. Pajchel, Single arrival kirchhoff prestack depth migration of complex faulted folds from the zagros mountains, iran, *Recorder*, *3*(1), 2006.

Blewett, R. S., Archaean tectonic processes: a case for horizontal shortening in the North Pilbara Granite-Greenstone Terrane, Western Australia, *Precambrian Research*, *113*(1), 87–120, doi:https://doi.org/10.1016/S0301-9268(01)00204-2, 2002.

Brown, M., Duality of thermal regimes is the distinctive characteristic of plate tectonics since the Neoarchean, *Geology*, *34*(11), 961, doi:10.1130/G22853A.1, 2006.

Brown, M., C. Kirkland, and T. Johnson, Evolution of geodynamics since the Archean: Significant change at the dawn of the Phanerozoic, *Geology*, *48*(5), 488–492, doi:10.1130/G47417.1, 2020.

Calvert, A. J., E. W. Sawyer, W. J. Davis, and J. N. Ludden, Archaean subduction inferred from seismic images of a mantle suture in the Superior Province, *Nature*, *375*(6533), 670–674, doi:10.1038/375670a0, 1995.

Carr, L., C. Southby, D. Edwards, J. Anderson, and S. MacFarlane, Exploring for the future: Canning basin, kidson seismic survey (18ga-kb1) and geological interpretation record: 2022/016. geoscience australia, canberra, doi:http://dx.doi.org/10.11636/Record.2022.016, 2022.

Cavosie, A. J., J. W. Valley, S. A. Wilde, and E.I.M.F., Magmatic δ18O in 4400–3900 Ma detrital zircons: A record of the alteration and recycling of crust in the Early Archean,

Earth and Planetary Science Letters, *235*(3), 663–681, doi:https://doi.org/10.1016/j.epsl.2005.04.028, 2005.

Cawood, P. A., A. Kröner, and S. Pisarevsky, Precambrian plate tectonics: Criteria and evidence, *GSA Today*, *16*(7), 4, doi:10.1130/GSAT01607.1, 2006.

Christensen, N. I., and W. D. Mooney, Seismic velocity structure and composition of the continental crust: A global view, *Journal of Geophysical Research: Solid Earth*, *100*(B6), 9761–9788, doi:10.1029/95JB00259, 1995.

Collins, W. J., Polydiapirism of the Archean Mount Edgar Batholith, Pilbara Block, Western Australia, *Precambrian Research*, *43*(1-2), 41–62, doi:10.1016/0301-9268(89)90004-1, 1989.

Collins, W. J., and M. J. Van Kranendonk, Model for the development of kyanite during partial convective overturn of Archean granite-greenstone terranes: The Pilbara Craton, Australia, *Journal of Metamorphic Geology*, *17*(2), 145–156, doi:10.1046/j.1525-1314.1999.00187.x, 1989.

Condie, K. C., High field strength element ratios in Archean basalts: a window to evolving sources of mantle plumes?, *Lithos*, *79*(3), 491–504, doi:https://doi.org/10.1016/j.lithos.2004.09.014, 2005.

Condie, K. C., and A. Kroner, When did plate tectonics begin? Evidence from the geologic record, in *Special Paper 440: When Did Plate Tectonics Begin on Planet Earth?*, vol. 440, pp. 281–294, Geological Society of America, doi:10.1130/2008.2440(14), 2008.

Dhuime, B., C. J. Hawkesworth, P. A. Cawood, and C. D. Storey, A Change in the Geodynamics of Continental Growth 3 Billion Years Ago, *Science*, *335*(6074), 1334–1336, doi:10.1126/science.1216066, 2012.

Doublier, M. P., et al., Basement architecture from the Pilbara Craton to the Aileron Province : new insights from deep seismic reflection line 18GA-KB1 Basement architecture from the Pilbara Craton to the Aileron Province : new insights from deep seismic reflection line 18GA-KB1, doi:10.11636/134381, 2020.

Foley, B. J., The dependence of planetary tectonics on mantle thermal state: applications to early Earth evolution, *Philosophical Transactions of the Royal Society A: Mathematical, Physical and Engineering Sciences*, *376*(2132), 20170,409, doi:10.1098/rsta.2017.0409, 2018.

Fomin, T., and R. D. Costelloe, L211 Kidson Sub-Basin 2D Seismic Survey, doi:10.26186/5ce72371e5b4c, 2019.

Francois, C., P. Philippot, P. Rey, and D. Rubatto, Burial and exhumation during Archean sagduction in the East Pilbara Granite-Greenstone Terrane, *Earth and Planetary Science Letters*, *396*, 235–251, doi:10.1016/j.epsl.2014.04.025, 2014.

Goodwin, A. M., *Principles of Precambrian Geology*, Academic Press, doi:https://doi.org/10.1016/B978-0-12-289770-2.X5000-6, 1996.

Hale, D., N. R. Hill, and J. P. Stefani, Imaging salt with turning seismic waves, *Geophysics*, *57*(11), 1171–1174, doi:10.1190/1.1888703, 1992.

Harrison, M. T., The hadean crust: Evidence from >4 ga zircons, *Annual Review of Earth and Planetary Sciences*, *37*, 479–505, doi:10.1146/annurev.earth.031208.100151, 2009.

Hawkesworth, C. J., P. A. Cawood, B. Dhuime, and T. I. Kemp, Earth's Continental Lithosphere Through Time, *Annual Review of Earth and Planetary Sciences*, *45*(1), 169–198, doi:10.1146/annurev-earth-063016-020525, 2017.

Hickman, A. H., Review of the Pilbara Craton and Fortescue Basin, Western Australia: Crustal evolution providing environments for early life, *Island Arc*, *21*(1), 1–31, doi:10.1111/j.1440-1738.2011.00783.x, 2012.

Hickman, A. H., and M. J. Van Kranendonk, *Diapiric processes in the formation of Archean continental crust, East Pilbara Granite-Greenstone Terrane, Australia*, pp. 118–139, 2004.

Hickman, A. H., and M. J. Van Kranendonk, Early Earth evolution: Evidence from the 3.5-1.8 Ga geological history of the Pilbara region of Western Australia, *Episodes*, *35*, 283–297, doi:10.18814/epiiugs/2012/v35i1/028, 2012.

Hickman, A. M., *Archaean diapirism in the Pilbara Block, Western Australia*, pp. 113–127, 1984.

Hole, J. A., Nonlinear High-Resolution Three-Dimensional Seismic Travel Time Tomography, *Journal of Geophysical Research*, *97*(B5), 6553–6562, 1992.

Hole, J. A., H. Thybo, and S. L. Klemperer, Seismic reflections from the near-vertical san andreas fault, *Geophysical Research Letters*, *23*(3), 237–240, doi:https://doi.org/10.1029/96GL00019, 1996.

Hole, J. A., R. D. Catchings, K. C. Clair, M. J. Rymer, D. A. Okaya, and B. J. Carney, Steep-dip seismic imaging of the shallow San Andreas fault near Parkfield, *Science*, *294*(5546), 1513–1515, doi:10.1126/science.1065100, 2001.

Hopkins, M. D., M. T. Harrison, and C. E. Manning, Low heat flow inferred from >4 Gyr zircons suggests Hadean plate boundary interactions, *Nature*, *456*(7221), 493–496, doi:10.1038/nature07465, 2008.

Hopkins, M. D., M. T. Harrison, and C. E. Manning, Constraints on Hadean geodynamics

from mineral inclusions in >4Ga zircons, *Earth and Planetary Science Letters*, *298*(3-4), 367–376, doi:10.1016/j.epsl.2010.08.010, 2010.

Kearey, P., K. A. Klepeis, and F. J. Vine, *Global Tectonics*, 3 ed., 496 pp., Wiley-Blackwell, doi:10.1126/science.168.3936.1250, 2009.

Kloppenburg, A., S. H. White, and T. E. Zegers, Structural evolution of the Warrawoona Greenstone Belt and adjoining granitoid complexes, Pilbara Craton, Australia: implications for Archaean tectonic processes, *Precambrian Research*, *112*(1), 107–147, doi:https://doi.org/10.1016/S0301-9268(01)00172-3, 2001.

Korenaga, J., Initiation and Evolution of Plate Tectonics on Earth: Theories and Observations, *Annual Review of Earth and Planetary Sciences*, *41*(1), 117–151, doi:10.1146/annurev-earth-050212-124208, 2013.

Kusky, T. M., and A. Polat, Growth of granite-greenstone terranes at convergent margins, and stabilization of Archean cratons, *Tectonophysics*, *305*(1-3), 43–73, doi:10.1016/S0040-1951(99)00014-1, 1999.

Martin, H., The mechanisms of petrogenesis of the Archaean continental crust—Comparison with modern processes, *Lithos*, *30*(3), 373–388, doi:https://doi.org/10.1016/0024-4937(93)90046-F, 1993.

Moore, W. B., and A. A. G. Webb, Heat-pipe earth, *Nature*, *501*(7468), 501–505, doi:10.1038/nature12473, 2013.

Nutman, A. P., C. R. L. Friend, and V. C. Bennett, Evidence for 3650-3600 Ma assembly of the northern end of the Itsaq Gneiss Complex, Greenland: Implication for early Archaean tectonics, *Tectonics*, *21*(1), 5–1–5–28, doi:10.1029/2000TC001203, 2002.

Roberts, N. M., B. Tikoff, and R. A. Salerno, Greenstone-Up Shear Sense at the Margin of the Mt Edgar Dome, East Pilbara Terrane: Implications for Dome and Keel Formation in the Early Earth, *Tectonics*, *41*(4), 1–20, doi:10.1029/2021TC007042, 2022.

Shirey, S. B., B. S. Kamber, M. J. Whitehouse, P. A. Mueller, and A. R. Basu, A review of the isotopic and trace element evidence for mantle and crustal processes in the Hadean and Archean: Implications for the onset of plate tectonic subduction, in *Special Paper 440: When Did Plate Tectonics Begin on Planet Earth?*, vol. 440, pp. 1–29, Geological Society of America, doi:10.1130/2008.2440(01), 2008.

Smithies, R. H., M. J. Van Kranendonk, and D. C. Champion, It started with a plume – early Archaean basaltic proto-continental crust, *Earth and Planetary Science Letters*, *238*(3), 284–297, doi:https://doi.org/10.1016/j.epsl.2005.07.023, 2005.

Smithies, R. H., M. J. Van Kranendonk, and D. C. Champion, The Mesoarchean emergence of modern-style subduction, *Gondwana Research*, *11*(1), 50–68, doi:https://doi.org/10.1016/j.gr.2006.02.001, 2007.

Stern, R. J., Evidence from ophiolites, blueschists, and ultrahigh-pressure metamorphic terranes that the modern episode of subduction tectonics began in Neoproterozoic time, *Geology*, *33*(7), 557, doi:10.1130/G21365.1, 2005.

Tang, M., K. Chen, and R. L. Rudnick, Archean upper crust transition from mafic to felsic marks the onset of plate tectonics, *Science*, *351*(6271), 372–375, doi:10.1126/science.aad5513, 2016.

Turner, S., T. Rushmer, M. Reagan, and J. F. Moyen, Heading down early on? Start of subduction on Earth, *Geology*, *42*(2), 139–142, doi:10.1130/G34886.1, 2014.

Van Kranendonk, M. J., Volcanic degassing, hydrothermal circulation and the flourishing of

early life on Earth: A review of the evidence from c. 3490-3240 Ma rocks of the Pilbara Supergroup, Pilbara Craton, Western Australia, *Earth-Science Reviews*, *74*(3), 197–240, doi:https://doi.org/10.1016/j.earscirev.2005.09.005, 2006.

Van Kranendonk, M. J., R. H. Smithies, A. H. Hickman, and D. C. Champion, Review: Secular tectonic evolution of Archean continental crust: interplay between horizontal and vertical processes in the formation of the Pilbara Craton, Australia, *Terra Nova*, *19*(1), 1–38, doi:10.1111/j.1365-3121.2006.00723.x, 2007.

Van Kranendonk, M. J., R. Hugh Smithies, A. H. Hickman, M. T. Wingate, and S. Bodorkos, Evidence for Mesoarchean (3.2Ga) rifting of the Pilbara Craton: The missing link in an early Precambrian Wilson cycle, *Precambrian Research*, *177*(1-2), 145–161, doi:10.1016/j.precamres.2009.11.007, 2010.

White, D. J., G. Musacchio, H. H. Helmstaedt, R. M. Harrap, P. C. Thurston, A. van der Velden, and K. Hall, Images of a lower-crustal oceanic slab: Direct evidence for tectonic accretion in the Archean western Superior province, *Geology*, *31*(11), 997–1000, doi:10.1130/G20014.1, 2003.

Williams, I. R., and A. H. Hickman, Nullagine, w.a. sheet sf 51-5: Western australia geological survey, 1:250Ý000 geological series, 2007.

Windley, B. F., and D. Bridgwater, The evolution of archaean low-and high grade terrains, 1971.

Yilmaz, O., *Seismic Data Analysis*, 2065 pp., Society of Exploration Geophysicists, doi:http://dx.doi.org/10.1190/1.9781560801580, 2001.

Zegers, T. E., S. H. White, M. de Keijzer, and P. Dirks, Extensional structures during deposition of the 3460 Ma Warrawoona Group in the eastern Pilbara Craton, Western Aus-

tralia, *Precambrian Research*, *80*(1), 89–105, doi:https://doi.org/10.1016/S0301-9268(96)00007-1, 1996.

Zelt, C. A., Modelling strategies and model assessment for wide-angle seismic traveltime data, *Geophysical Journal International*, *139*(1), 183–204, doi:10.1046/j.1365-246X.1999.00934.x, 1999.

Appendices

Appendix A

Geologic Timescale

Eon	Era	Date (MYA)
Phanerozoic		541-current
Proterozoic	Neoproterozoic	1,000 to 541
	Mesoproterozoic	1,600 to 1,000
	Paleoproterozoic	2,500 to 1,600
Archean	Neoarchean	2,800 to 2,500
	Mesoarchean	3,200 to 2,800
	Paleoarchean	3,600 to 3,200
	Eoarchean	4,000 to 3,600
Hadean		pre-4,000

Table A.1: Geologic Timescale

Appendix B

Permissions for Figures

Figure 7.1. Based on "Early Earth evolution: evidence from the 3.5–1.8 Ga geological history of the Pilbara region of Western Australia" by Arthur H. Hickman and Martin J. Van Kranendonk and is provided under a Creative Commons Attribution 4.0 International License and is subject to the disclaimer of warranties in section 5 of that license. https://doi.org/10.18814/epiiugs/2012/v35i1/028

Figure 7.2. Based on "Growth of granite-greenstone terranes at convergent margins, and stabilization of Archean cratons" by Timothy M. Kusky and Ali Polat and is provided under a Creative Commons Attribution 4.0 International Licence and is subject to the disclaimer of warranties in section 5 of that licence. https://www.researchgate.net/publication/222116413.

Figure 7.10. Based on "Basement architecture from the Pilbara Craton to the Aileron Province: new insights from deep seismic reflection line 18GA-KB1." By Geoscience Australia which is ©Commonwealth of Australia and is provided under a Creative Commons Attribution 4.0 International Licence and is subject to the disclaimer of warranties in section 5 of that licence. http://dx.doi.org/10.11636/134381.

Figure 7.11. Based on "Basement architecture from the Pilbara Craton to the Aileron Province: new insights from deep seismic reflection line 18GA-KB1." By Geoscience Australia which is ©Commonwealth of Australia and is provided under a Creative Commons Attribution 4.0 International Licence and is subject to the disclaimer of warranties in sec-